mathematics

MDPI

Article

Three-Dimensional Magnetotelluric Forward Modeling in the Mixed Space-Wavenumber Domain with Divergence Correction

Tiegang Tong †, Yufei Yang † and Diquan Li *

School of Geosciences and Info-Physics, Central South University, Changsha 410083, China; tongtiegang@csu.edu.cn (T.T.); 255011098@csu.edu.cn (Y.Y.)
* Correspondence: lidiquan@csu.edu.cn
† These authors contributed equally to this work.

Abstract

Three-dimensional magnetotelluric (MT) forward modeling remains constrained by the difficulty of achieving both high numerical accuracy and computational efficiency. To address this limitation, we propose a mixed space-wavenumber domain method based on coupled equations for the magnetic vector potential and electric scalar potential under the Lorenz gauge. Our method incorporates a divergence correction scheme and employs the Gaussian Fourier transform technique to solve the three-dimensional MT forward problem. The vector-potential equation reduces the number of unknowns and computational cost, while simplifying the treatment of boundary conditions at conductivity interfaces. The divergence correction suppresses spurious solutions at anomalous-body boundaries in low-induction-number regimes. We use Gauss-FFT instead of the traditional FFT to reduce the errors due to aliasing and imposed periodicity as well as edge effects in the MT forward modeling. Numerical experiments demonstrate that both iterative solution time and memory consumption scale linearly with the number of computational nodes. On refined meshes, the proposed method requires approximately one-eighth of the iterative solution time and one-quarter of the memory required by the finite element method. Together, these improvements substantially enhance computational efficiency without compromising numerical accuracy. The method is therefore well suited for large-scale 3D MT forward modeling on laterally regular grids with layered or vertically heterogeneous media, as required in high-resolution mineral exploration and regional crustal-structure imaging, where both accuracy and efficiency are essential.

Keywords: magnetotelluric method; 3D forward modeling; mixed space-wavenumber domain; divergence correction; Gauss–FFT

MSC: 86A25

Check for updates

Academic Editors: Baccouch Mahboub and Yiu Yin Raymond Lee

Received: 9 September 2026
Revised: 9 October 2026
Accepted: 22 October 2026
Published: 27 October 2026

Copyright: © 2026 by the authors. Licensee MDPI, Basel, Switzerland. This article is an open access article distributed under the terms and conditions of the Creative Commons Attribution (CC BY) license.

1. Introduction

The magnetotelluric (MT) method employs electromagnetic (EM) fields originating from space and ionospheric activities as its excitation source [1,2]. By approximating the impinging EM waves at the Earth's surface as plane waves, the technique leverages the principle of electromagnetic induction to characterize the spatial and temporal distributions of measured EM fields, enabling effective subsurface target detection [3,4]. To achieve high-resolution, deep-penetration multi-parameter exploration under complex geological settings, robust, efficient, and highly accurate EM forward modeling algorithms serve as a critical foundation for reliable geophysical inversion [5]. Given that conventional 1D

and 2D forward frameworks no longer meet the requirements for fine-scale subsurface characterization [6,7], thus there is significantly increased interest and awareness in 3D modelling and inversion, and the efforts to develop 3D codes have increased [8].

In the context of MT forward modeling, numerical approaches are generally categorized by their mathematical formulation into two major families [9,10]: differential equation (DE)-based methods, represented by finite difference (FDM), finite element (FEM), and finite volume (FVM) schemes, and integral equation (IE)-based methods.

The integral equation method was first introduced to EM field problems by Dmitriev [11], and subsequently matured through systematic developments by Hohmann, Wannamaker, and other researchers [12–15]. Later advances include an optimization algorithm developed by Avdeev and Knizhnik [16] based on the decomposability of tensor Green's functions, a hybrid spatial-wavenumber domain Green's function calculation scheme proposed by Zhang et al. [17] to enhance computational efficiency, a tetrahedral-mesh implementation paired with the PARDISO parallel direct solver by Ren et al. [18], and a symmetry group representation technique described by Ma et al. [19] to reduce the cost of matrix element assembly. Nevertheless, the IE approach requires storage of dense full-rank Green's function matrices, with memory scaling cubically with model size, which severely limits its applicability to large-scale 3D MT problems.

The finite difference method, the earliest DE-based numerical scheme, forms the core kernel of widely used inversion frameworks such as ModEM. Lines and Jones first adapted FDM for MT forward modeling [20], followed by the pioneering work of Mackie that integrated staggered-grid FDM with conjugate gradient inversion [21]. The generalized "incomplete Cholesky preconditioning + divergence correction" framework was later formulated by Mackie et al., and further refined for practical implementation by Tan and Chen et al. [9,22,23], while Newman and Alumbaugh developed a standard parallelization architecture for distributed computing [24]. However, conventional FDM commonly uses structured orthogonal meshes, although unstructured/multi-resolution FDM variants have been developed [25]., which limits its capability to accurately represent rugged topography and complex geological structures; additionally, extra iterative steps for divergence correction add non-negligible overhead to the overall simulation workflow.

The finite element method (FEM), owing to its flexible meshing and good conformity to irregular topography, has become a mainstream tool for modern EM simulation. Coggon first introduced FEM to geophysical EM modeling [26], and Jin's vector FEM eliminated spurious non-physical solutions in earlier nodal implementations [27]. Tang et al. later developed a Coulomb-gauge adaptive FEM framework for high-precision MT simulation [28]. More recently, Grayver and Bürg [29] proposed a robust and scalable 3D geo-electromagnetic FEM solver using unstructured non-conforming hexahedral meshes and an optimal block-diagonal preconditioner, with iteration counts nearly independent of problem size up to 200 million unknowns; Grayver and Kolev [30] further extended it to parallel adaptive high-order FEM, showing lower computational cost and fewer degrees of freedom than lowest-order adaptive FEM for high accuracy; and Grayver [31] developed a distributed adaptive-FEM 3D MT inversion with decoupled forward/inverse meshes and automatic refinement. Nevertheless, the FEM stiffness matrix, though sparse, remains extremely large-scale, and the preprocessing and computational costs of unstructured meshes are still prohibitive for large 3D forward modeling campaigns.

The finite volume method sits conceptually between FDM and FEM, combining clear physical conservation principles and competitive numerical accuracy. Haber and Ascher developed Coulomb-gauge based 3D FVM for EM simulation [32], Weiss implemented a parallel FVM solver under the Lorenz gauge [33], and Jahandari and Farquharson extended the scheme to accommodate unstructured meshes for complex heterogeneous media [34].

To date, however, FVM for 3D MT has not evolved into a fully mature, community-validated software ecosystem comparable to established platforms such as ModEM or MT-Pioneer, and its performance remains to be further improved for specialized applications including large-scale anisotropic modeling and topography-coupled inversion.

Beyond these four main approaches, the spectral element method and the mesh-free method have also been developed [35–37]. Recent reviews have further emphasized the importance of scalable numerical grids and efficient solvers for 3D electromagnetic forward modeling. In particular, Wang et al. [38] reviewed efficient multigrid algorithms for 3D electromagnetic forward modeling and highlighted their potential for large-scale problems. Nevertheless, all existing mainstream methods share well-recognized inherent limitations: the IE method is fundamentally constrained by the background Green's function equation and dense matrix storage, making it difficult to support large-scale 3D inversion. Differential-equation-based methods, while free of Green-function dependencies, require full-domain discretization that inevitably produces a huge number of unknowns; they also suffer from common errors such as truncation-boundary errors and spurious solutions in the low-induction-number regime [39]. Meanwhile, FDM and FEM involve trade-off between topographic flexibility and computational cost.

To address these unresolved issues, this work builds on the previous established a mixed space-wavenumber domain forward modeling [40–42], but advances them in two key aspects. First, unlike the previous studies, where the vector-potential formulation did not explicitly enforce the divergence-free condition at conductivity interfaces, we introduce a divergence-correction scheme directly into the coupled vector-potential and scalar-potential equations. This suppresses spurious space-charge accumulation and non-physical boundary oscillations in low-induction-number regimes. Second, instead of the conventional FFT used in Dai et al., we adopt a two-dimensional Gauss-Legendre FFT for horizontal wavenumber integration, which reduces aliasing, imposed periodicity, and spectral truncation errors without increasing the number of sampling points. These improvements extend the previous mixed-domain framework to accurate and efficient 3D MT forward modeling.

2. Governing Equations and Numerical Methods

2.1. Mixed Space-Wavenumber Domain Vector-Field Governing Equations

In this work, the medium is assumed to be non-magnetic, with constant magnetic permeability and dielectric permittivity equal to their respective vacuum values, i.e., $\mu = \mu_0 =$ constant and $\varepsilon = \varepsilon_0 =$ constant, while the electrical conductivity $\sigma(\mathbf{r})$ may vary spatially. The time-harmonic convention $e^{i\omega t}$ is adopted throughout. In the magnetotelluric (MT) frequency band, displacement currents are generally negligible in the conductive Earth. However, they are retained in the following derivation for completeness unless explicitly neglected.

$$\begin{cases} \nabla \times \mathbf{H} = \mathbf{J}_e + (\sigma + i\varepsilon_0\omega)\mathbf{E} \\ \nabla \times \mathbf{E} = -i\mu_0\omega\mathbf{H} \\ \nabla \cdot \mathbf{H} = 0 \\ \nabla \cdot \mathbf{E} = \frac{\rho}{\varepsilon_0} \end{cases} \tag{1}$$

where $\mathbf{E}$ and $\mathbf{H}$ denote the electric field and the magnetic field, and $\mathbf{J}_e$ denotes the frequency-domain expression for the applied current source.

Unlike the method of directly solving for the electric and magnetic field quantities used by Wang et al. [43], our work starts from the vector-potential and scalar-potential

equations satisfied by the electric and magnetic fields. Equation (1) can be expressed in terms of the vector potential $\mathbf{A}$ and scalar potential ϕ as:

$$\mathbf{B} = \nabla \times \mathbf{A},\ \mathbf{H} = \frac{1}{\mu_0}\nabla \times \mathbf{A} \tag{2}$$

$$\mathbf{E} = -i\omega\mathbf{A} - \nabla\varphi \tag{3}$$

It should be noted that the vector potential and scalar potential here are both functions of time and space. When neither depends on time, the relationships between the vector potential, scalar potential, and field quantities are completely consistent with those in static fields. Therefore, the vector potential is also called the vector magnetic potential, and the scalar potential is also called the scalar electric potential.

Using the vector identity $\nabla\times\nabla\times\mathbf{A}=\nabla(\nabla\cdot\mathbf{A}) - (\nabla^2\mathbf{A})$, we obtain:

$$\nabla(\nabla\cdot\mathbf{A}) - \nabla^2\mathbf{A} + (i\sigma\mu_0\omega - \mu_0\varepsilon_0\omega^2)\mathbf{A} + \mu_0(\sigma + i\varepsilon\omega)\nabla\varphi = \mu_0\mathbf{J}_e \tag{4}$$

When $\mathbf{J}_e = 0$, the above equation becomes the governing equation satisfied by the vector potential and scalar potential in magnetotelluric problems.

The secondary-field method is used to solve for the electromagnetic-field vector potential, separating the background field from the anomalous field. The governing equations satisfied by the vectorpotential and scalar potential of the background field can be written as:

$$\nabla(\nabla\cdot\mathbf{A}^b) - \nabla^2\mathbf{A}^b + (i\sigma_b\mu_0\omega - \mu_0\varepsilon_0\omega^2)\mathbf{A}^b + \mu_0(\sigma_b + i\varepsilon_0\omega)\nabla\varphi^b = 0 \tag{5}$$

where $\mathbf{A}^b$ represents the background field vector, φ^b represents the scalar component of the background field, and σ_b represents the background field conductivity.

Let $\mathbf{J}_s = \sigma_s E$, where $\mathbf{J}_s$ denotes the abnormal current density. The governing equation satisfied by the vector potential and scalar potential of the secondary field can be written as:

$$\nabla(\nabla\cdot\mathbf{A}^s) - \nabla^2\mathbf{A}^s + (i\sigma_b\mu_0\omega - \mu_0\varepsilon_0\omega^2)\mathbf{A}^s + \mu_0(\sigma_b + i\varepsilon_0\omega)\nabla\varphi^s = \mu_0\mathbf{J}_s \tag{6}$$

In the Equation (6), $\mathbf{A}^s$ represents the vector component of the secondary field, φ^srepresents the scalar component of the secondary field, and $\sigma_b = \sigma - \sigma_s$ represents the anomalous conductivity.

Using the Lorenz gauge:

$$\nabla\cdot\mathbf{A}^s + \mu_0(\sigma_b + i\varepsilon_0\omega)\nabla\varphi^s = 0 \tag{7}$$

Let the wavenumber of the electromagnetic field be $k_s = \sqrt{-(i\sigma_b\mu_0\omega - \mu_0\varepsilon_0\omega^2)}$. Then, the above equation can be simplified as:

$$\nabla^2\mathbf{A}^s + k_s A^s = -\mu_0\mathbf{J}_s \tag{8}$$

Assuming that the medium is non-magnetic ($\mu = \mu_0 = 1$) and that the permittivity equals that of free space, Equation (8) is expanded into three component equations along the x, y, and z directions:

$$\begin{cases} \frac{\partial^2\mathbf{A}_x^s}{\partial x^2} + \frac{\partial^2\mathbf{A}_x^s}{\partial y^2} + \frac{\partial^2\mathbf{A}_x^s}{\partial z^2} + k_s^2\mathbf{A}_x^s = -\mathbf{J}_{sx} \\ \frac{\partial^2\mathbf{A}_y^s}{\partial x^2} + \frac{\partial^2\mathbf{A}_y^s}{\partial y^2} + \frac{\partial^2\mathbf{A}_y^s}{\partial z^2} + k_s^2\mathbf{A}_y^s = -\mathbf{J}_{sy} \\ \frac{\partial^2\mathbf{A}_z^s}{\partial x^2} + \frac{\partial^2\mathbf{A}_z^s}{\partial y^2} + \frac{\partial^2\mathbf{A}_z^s}{\partial z^2} + k_s^2\mathbf{A}_z^s = -\mathbf{J}_{sz} \end{cases} \tag{9}$$

where $\mathbf{A}_x^s$, $\mathbf{A}_y^s$ and $\mathbf{A}_z^s$ represent the secondary field vector potentials in the x, y, and z directions, and $\mathbf{J}_{sx}$, $\mathbf{J}_{sy}$ and $\mathbf{J}_{sz}$ represent the abnormal current density in the x, y, and z directions. Equation (9) represents the governing equations for the vector components

of the secondary electromagnetic field under the Lorenz gauge. Its primary advantage lies in the absence of scalar components, resulting in a more concise equation form and a significant reduction in computational load. Furthermore, the governing equations for the three vector components $\mathbf{A}_x^s$, $\mathbf{A}_y^s$ and $\mathbf{A}_z^s$ are completely decoupled and can be solved independently, greatly reducing the dimensionality of each sub-system of equations and thereby effectively improving overall computational efficiency.

Applying the two-dimensional Fourier transform in the horizontal direction to Equation (9), and letting $c = \sqrt{\hat{k}_x^2 + \hat{k}_y^2 - k_s^2}$, we obtain:

$$\begin{cases} \frac{\partial^2 \hat{\mathbf{A}}_x^s}{\partial z^2} - c^2 \hat{\mathbf{A}}_x^s = -\hat{\mathbf{J}}_{sx} \\ \frac{\partial^2 \hat{\mathbf{A}}_y^s}{\partial z^2} - c^2 \hat{\mathbf{A}}_y^s = -\hat{\mathbf{J}}_{sy} \\ \frac{\partial^2 \hat{\mathbf{A}}_z^s}{\partial z^2} - c^2 \hat{\mathbf{A}}_z^s = -\hat{\mathbf{J}}_{sz} \end{cases} \tag{10}$$

where $\hat{\mathbf{A}}_x^s$, $\hat{\mathbf{A}}_y^s$ and $\hat{\mathbf{A}}_z^s$ represent the corresponding mixed space-wavenumber domain vector potentials, obtained from the vector potentials $\mathbf{A}_x^s$, $\mathbf{A}_y^s$ and $\mathbf{A}_z^s$ through a two-dimensional Fourier transform in the horizontal direction. $\hat{k}_x^2$ and $\hat{k}_y^2$ represent the wavenumbers corresponding to the Fourier transforms in the horizontal direction x and the vertical direction y. $\hat{\mathbf{J}}_{sx}$, $\hat{\mathbf{J}}_{sy}$ and $\hat{\mathbf{J}}_{sz}$ represent the mixed space-wavenumber domain secondary-field current densities, obtained from the space domain $\mathbf{J}_{sx}$, $\mathbf{J}_{sx}$ and $\mathbf{J}_{sz}$ through a two-dimensional Fourier transform in the horizontal direction.

Appropriate boundary conditions must be applied when solving the Equation (10), the derivation process for the upper and lower boundary conditions is detailed below. When the boundary is set to a region free of anomalies, the right-hand side of equation is zero, and its general solution can be written $\hat{\mathbf{A}}_x^s = Ae^{cz} + Be^{-cz}$. According to the kinematic principles of electromagnetic wave propagation, to ensure that the wavefield satisfies the attenuation condition, only upward waves exist at the upper boundary and only downward waves exist at the lower boundary. Thus, the boundary conditions for the quadratic field vector in the mixed space-wavenumber domain are:

Upper boundary condition:

$$\begin{cases} \frac{\partial \hat{\mathbf{A}}_x^s}{\partial z}\Big|_{z=z_{min}} = c_t \hat{\mathbf{A}}_x^s \\ \frac{\partial \hat{\mathbf{A}}_y^s}{\partial z}\Big|_{z=z_{min}} = c_t \hat{\mathbf{A}}_y^s \\ \frac{\partial \hat{\mathbf{A}}_z^s}{\partial z}\Big|_{z=z_{min}} = c_t \hat{\mathbf{A}}_z^s \end{cases} \tag{11}$$

In the Equation (11), $c_t = \sqrt{\hat{k}_x^2 + \hat{k}_y^2 - k_{st}^2}$ and $k_{st} = \sqrt{-(i\sigma_{bt}\mu_0\omega - \mu_0\varepsilon_0\omega^2)}$ represent the wave numbers of the electromagnetic field corresponding to the layer where the lower boundary is located, and σ_{bt} represents the background electrical conductivity of the electromagnetic field corresponding to that layer.

Lower boundary conditions:

$$\begin{cases} \frac{\partial \hat{\mathbf{A}}_x^s}{\partial z}\Big|_{z=z_{max}} = -c_B \hat{\mathbf{A}}_x^s \\ \frac{\partial \hat{\mathbf{A}}_y^s}{\partial z}\Big|_{z=z_{max}} = -c_B \hat{\mathbf{A}}_y^s \\ \frac{\partial \hat{\mathbf{A}}_z^s}{\partial z}\Big|_{z=z_{max}} = -c_B \hat{\mathbf{A}}_z^s \end{cases} \tag{12}$$

In the Equation (12), $c_B = \sqrt{\hat{k}_x^2 + \hat{k}_y^2 - k_{sb}^2}$ and $k_{sb} = \sqrt{-(i\sigma_{bb}\mu_0\omega - \mu_0\varepsilon_0\omega^2)}$ represent the wave numbers of the electromagnetic field corresponding to the layer where the lower boundary is located, and σ_{bb} represents the background electrical conductivity of the electromagnetic field corresponding to that layer.

2.2. Divergence Correction

At the interface between media with different electrical properties, the electromagnetic field must satisfy three fundamental boundary conditions: continuity of the tangential component of the electric field, continuity of the normal component of the current density, and continuity of the normal component of the magnetic flux density [44]. Based on Maxwell's equations, the magnetic flux continuity condition $\nabla \cdot \mathbf{B} = 0$ requires, under the quasi-static approximation, that the vector potential $\mathbf{A}$ satisfy $\nabla \cdot \mathbf{A} = 0$ (i.e., the Lorenz condition). However, when directly solving the vector potential governing equations, if the conductivities on either side of the dielectric interface differ significantly, the ability of the discrete system to maintain this divergence-free constraint decreases significantly [45,46]. Specifically, when numerical solutions obtained via finite element or finite difference discretization cross an electrical interface, the basis functions or difference schemes cannot precisely satisfy the normal continuity of current density at the interface. This leads to the accumulation of residuals where $\nabla \cdot \mathbf{A} \neq 0$, which in turn generates spurious space charge accumulation. These numerical pseudo-solutions manifest as non-physical oscillations in the electric or magnetic fields near the boundaries of the anomalous region, severely affecting the accuracy of forward simulation results [47,48].

To fundamentally suppress such spurious solutions, it is necessary to introduce divergence boundary conditions on the electrical interface that match the dielectric layering, thereby enforcing strict compliance with the Lorenz normalization. After adding these conditions to the vector potential governing equations, the horizontal electric fields $\mathbf{E}_x$, $\mathbf{E}_y$ and the horizontal magnetic fields $\mathbf{H}_x$, $\mathbf{H}_y$ are continuous, while the vertical electric field $\mathbf{E}_z$ is discontinuous. Based on the relationship between the vector potential and the electromagnetic fields as defined by the Lorenz condition, the boundary of the anomalous body satisfies the following three relationships:

$$\begin{cases} \hat{\mathbf{A}}_{x1}^{s} = \hat{\mathbf{A}}_{x2}^{s} \\ \frac{\partial \hat{\mathbf{A}}_{x1}^{s}}{\partial z} = \frac{\partial \hat{\mathbf{A}}_{x2}^{s}}{\partial z} \end{cases} \tag{13}$$

$$\begin{cases} \hat{\mathbf{A}}_{y1}^{s} = \hat{\mathbf{A}}_{y2}^{s} \\ \frac{\partial \hat{\mathbf{A}}_{y1}^{s}}{\partial z} = \frac{\partial \hat{\mathbf{A}}_{y2}^{s}}{\partial z} \end{cases} \tag{14}$$

$$\begin{cases} \hat{\mathbf{A}}_{z1}^{s} = \hat{\mathbf{A}}_{z2}^{s} \\ \frac{1}{\sigma_{B1}+i\varepsilon\omega}\left(ik_x\hat{\mathbf{A}}_{x1}^{s} + ik_y\hat{\mathbf{A}}_{y1}^{s} + \frac{\partial \hat{\mathbf{A}}_{z1}^{s}}{\partial z}\right) = \frac{1}{\sigma_{B2}+i\varepsilon\omega}\left(ik_x\hat{\mathbf{A}}_{x2}^{s} + ik_y\hat{\mathbf{A}}_{y2}^{s} + \frac{\partial \hat{\mathbf{A}}_{z2}^{s}}{\partial z}\right) \end{cases} \tag{15}$$

where $\hat{\mathbf{A}}_{x1}^{s}$, $\hat{\mathbf{A}}_{y1}^{s}$ and $\hat{\mathbf{A}}_{z1}^{s}$ represent the vector potential expressions in the mixed space-wavenumber domain at the upper interface of the layered medium; and σ_{b1} represents the background electrical conductivity at the upper interface of the layered medium; $\hat{\mathbf{A}}_{x2}^{s}$, $\hat{\mathbf{A}}_{y2}^{s}$ and $\hat{\mathbf{A}}_{z2}^{s}$ represent the vector potential expressions in the maxed space-wavenumber domain at the lower interface of the layered medium; and σ_{b2} represents the background electrical conductivity at the lower interface of the layered medium. Introducing divergence corrections at the interface between the anomalous body and the background field can effectively prevent the occurrence of spurious solutions.

2.3. Finite Element Method

The boundary value problem corresponding to Equation (10) is reformulated as the following three variational problems:

$$\begin{cases} F(\hat{\mathbf{A}}_x^{s}) = \int_{z_{min}}^{z_{max}} \left[\left(\frac{\partial \hat{\mathbf{A}}_x^{s}}{\partial z} \right)^2 + \left(C\hat{\mathbf{A}}_x^{s} \right)^2 - 2\hat{\mathbf{J}}_{sx}\hat{\mathbf{A}}_x^{s} \right] dz + C_T(\hat{\mathbf{A}}_x^{s}|_{z_{min}})^2 + C_{\mathbf{B}}(\hat{\mathbf{A}}_x^{s}|_{z_{max}})^2 \\ \delta F(\hat{\mathbf{A}}_x^{s}) = 0 \end{cases} \tag{16}$$

$$\begin{cases} F(\hat{\mathbf{A}}_y^s) = \int_{z_{min}}^{z_{max}} \left[\left(\frac{\partial \hat{\mathbf{A}}_y^s}{\partial z} \right)^2 + \left(c\hat{\mathbf{A}}_y^s \right)^2 - 2\hat{\mathbf{J}}_{sy}\hat{\mathbf{A}}_y^s \right] dz + c_t(\hat{\mathbf{A}}_y^s|_{z_{min}})^2 + c_b(\hat{\mathbf{A}}_y^s|_{z_{max}})^2 \\ \delta F(\hat{\mathbf{A}}_y^s) = 0 \end{cases} \tag{17}$$

$$\begin{cases} F(\hat{\mathbf{A}}_z^s) = \int_{z_{min}}^{z_{max}} \left[\left(\frac{\partial \hat{\mathbf{A}}_z^s}{\partial z} \right)^2 + \left(c\hat{\mathbf{A}}_z^s \right)^2 - 2\hat{\mathbf{J}}_{sz}\hat{\mathbf{A}}_z^s \right] dz + c_t(\hat{\mathbf{A}}_z^s|_{z_{min}})^2 + c_b(\hat{\mathbf{A}}_z^s|_{z_{max}})^2 \\ \delta F(\hat{\mathbf{A}}_z^s) = 0 \end{cases} \tag{18}$$

As shown in Equations (16)–(18), the boundary value problem is transformed into a variational problem, which is then solved using the finite element method. The finite element method employs natural coordinates (e.g., Figure 1), The one-dimensional natural coordinates and on the element are expressed as:

$$L_j = \frac{z_m - z}{l}, L_m = \frac{z - z_j}{l}, l = z_m - z_j, L_m = 1 - L_j \tag{19}$$

where z_j and z_m represent the coordinates of the start and end nodes of each element.

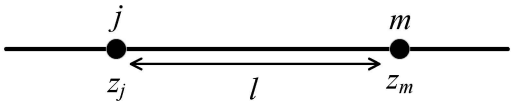


Figure 1. Schematic diagram of quadratic interpolation shape functions for 1D elements.

The solution domain is subdivided into N elements in the z-direction, and quadratic interpolation is then applied to each element. The quadratic interpolation function defined in terms of length coordinates can be written as:

$$N_j = (2L_j - 1)L_j, N_p = 4L_jL_m, N_m = (2L_m - 1)L_m \tag{20}$$

where N_j, N_p and N_m represent the coordinates of the start, middle, and end nodes of each element, as shown in Figure 2.

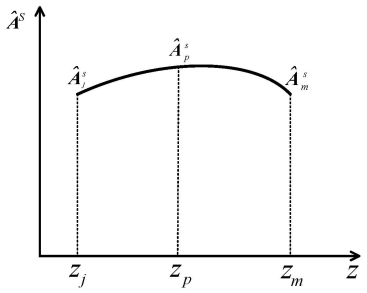


Figure 2. Schematic of vertical discretization with quadratic interpolation for vector potential.

The matrix form of each parameter within a cell is:

$$\begin{cases} \hat{\mathbf{A}}_x^s = \begin{pmatrix} N_j & N_p & N_m \end{pmatrix} \begin{pmatrix} \hat{\mathbf{A}}_{xj}^s & \hat{\mathbf{A}}_{xp}^s & \hat{\mathbf{A}}_{xm}^s \end{pmatrix}^T \\ \hat{\mathbf{A}}_y^s = \begin{pmatrix} N_j & N_p & N_m \end{pmatrix} \begin{pmatrix} \hat{\mathbf{A}}_{yj}^s & \hat{\mathbf{A}}_{yp}^s & \hat{\mathbf{A}}_{ym}^s \end{pmatrix}^T \\ \hat{\mathbf{A}}_z^s = \begin{pmatrix} N_j & N_p & N_m \end{pmatrix} \begin{pmatrix} \hat{\mathbf{A}}_{zj}^s & \hat{\mathbf{A}}_{zp}^s & \hat{\mathbf{A}}_{zm}^s \end{pmatrix}^T \\ c^2 = \begin{pmatrix} N_j & N_p & N_m \end{pmatrix} \begin{pmatrix} c_j^2 & c_p^2 & c_p^2 \end{pmatrix}^T \\ \hat{\mathbf{J}}_{sx} = \begin{pmatrix} N_j & N_P & N_m \end{pmatrix} \begin{pmatrix} \hat{\mathbf{J}}_{sxj} & \hat{\mathbf{J}}_{sxj} & \hat{\mathbf{J}}_{sxj} \end{pmatrix}^T \\ \hat{\mathbf{J}}_{sy} = \begin{pmatrix} N_j & N_P & N_m \end{pmatrix} \begin{pmatrix} \hat{\mathbf{J}}_{syj} & \hat{\mathbf{J}}_{syj} & \hat{\mathbf{J}}_{syj} \end{pmatrix}^T \\ \hat{\mathbf{J}}_{sz} = \begin{pmatrix} N_j & N_P & N_m \end{pmatrix} \begin{pmatrix} \hat{\mathbf{J}}_{szj} & \hat{\mathbf{J}}_{szj} & \hat{\mathbf{J}}_{szj} \end{pmatrix}^T \end{cases} \tag{21}$$

where j, p and m denote the start node, middle node, and end node of the element.

Taking the expression $\hat{\mathbf{A}}_x^s$ as an example, we perform a cell decomposition to break down the integral of the variational problem into integrals over individual cells. The integral for the i-th cell is:

$$\begin{aligned} F_i(\hat{\mathbf{A}}_x^s) &= \hat{\mathbf{A}}_x^s \left[\int_i \left(\frac{\partial N^T}{\partial z} \right) \left(\frac{\partial N}{\partial z} \right) dz \right] \left(\hat{\mathbf{A}}_x^s \right)^T \\ &+ \hat{\mathbf{A}}_x^s \left[\int_i \left(c^2 N^T N \right) dz \right] \left(\hat{\mathbf{A}}_x^s \right)^T - 2\hat{\mathbf{A}}_x^s \left[\int_i \left(N^T N \right) dz \right] \left(\hat{\mathbf{J}}_{sx}^s \right)^T \end{aligned} \tag{22}$$

where $N = (N_j \quad N_p \quad N_m)$, $\hat{\mathbf{A}}_x^s = (\hat{\mathbf{A}}_{xj}^s \quad \hat{\mathbf{A}}_{xp}^s \quad \hat{\mathbf{A}}_{xm}^s)$ and $\hat{\mathbf{J}}_{sx} = (\hat{\mathbf{J}}_{sxj} \quad \hat{\mathbf{J}}_{sxp} \quad \hat{\mathbf{J}}_{sxm})$.

For the first integral term in the Equation (22), the result is as follows:

$$K_{1i} = \int_i \left(\frac{\partial N^T}{\partial z} \right) \left(\frac{\partial N}{\partial z} \right) dz = \frac{1}{3l} \begin{pmatrix} 7 & -8 & 1 \\ -8 & 16 & -8 \\ 1 & -8 & 7 \end{pmatrix} \tag{23}$$

For the second integral in the Equation (22), the result is as follows:

$$K_{2i} = \int_i \left(c^2 N^T N \right) dz = \frac{l}{420} \begin{pmatrix} 39c_j^2 + 20c_p^2 - 3c_m^2 & 20c_j^2 + 16c_p^2 - 8c_m^2 & -3c_j^2 - 8c_p^2 - 3c_m^2 \\ 20c_j^2 + 16c_p^2 - 8c_m^2 & 16c_j^2 + 192c_p^2 + 16c_m^2 & -8c_j^2 + 16c_p^2 + 20c_m^2 \\ -3c_j^2 - 8c_p^2 - 3c_m^2 & -8c_j^2 + 16c_p^2 + 20c_m^2 & -3c_j^2 + 20c_p^2 + 39c_m^2 \end{pmatrix} \tag{24}$$

For the third integral in the Equation (22), the result is as follows:

$$p_i = \int_i \left(N^T N \right) dz = \frac{l}{30} \begin{pmatrix} 4 & 2 & -1 \\ 2 & 16 & 2 \\ -1 & 2 & 4 \end{pmatrix} \tag{25}$$

We sum the discrete integral units mentioned above:

$$F(\hat{\mathbf{A}}_x^s) = \hat{\mathbf{A}}_x^s \left(\sum_i^N K_{1i} \right) \left(\hat{\mathbf{A}}_x^s \right)^T + \hat{\mathbf{A}}_x^s \left(\sum_i^N K_{2i} \right) \left(\hat{\mathbf{A}}_x^s \right)^T - 2\hat{\mathbf{A}}_x^s \left(\sum_i^N P_{xi} \right) \left(\hat{\mathbf{J}}_{sx}^s \right)^T \tag{26}$$

At the same time, We substitute the boundary conditions of the first and last nodes, the results are as follows:

$$c_t (\hat{\mathbf{A}}_x^s|_{z_{min}})^2 = \hat{\mathbf{A}}_x^s \begin{bmatrix} c_t & \dots & 0 \\ \dots & \dots & \dots \\ 0 & \dots & 0 \end{bmatrix} \left(\hat{\mathbf{A}}_x^s \right)^T = \hat{\mathbf{A}}_x^s C_{x1} \left(\hat{\mathbf{A}}_x^s \right)^T \tag{27}$$

$$c_b (\hat{\mathbf{A}}_x^s|_{z_{max}})^2 = \hat{\mathbf{A}}_x^s \begin{bmatrix} 0 & \dots & 0 \\ \dots & \dots & \dots \\ 0 & \dots & c_b \end{bmatrix} \left(\hat{\mathbf{A}}_x^s \right)^T = \hat{\mathbf{A}}_x^s C_{x2} \left(\hat{\mathbf{A}}_x^s \right)^T \tag{28}$$

We compose the above matrix, given by:

$$F(\hat{\mathbf{A}}_x^s) = \hat{\mathbf{A}}_x^s \left(\sum_i^N K_{1i} + \sum_i^N K_{2i} + C_{x1} + C_{x2} \right) \left(\hat{\mathbf{A}}_x^s \right)^T - 2\hat{\mathbf{A}}_x^s \left(\sum_i^N P_{xi} \right) \left(\hat{\mathbf{J}}_{sx}^s \right)^T \tag{29}$$

Let $K_x = \left(\sum_i^N K_{1i} + \sum_i^N K_{2i} + C_{x1} + C_{x2} \right)$, $P_x = \left(\sum_i^N P_{xi} \right) \left(\hat{\mathbf{J}}_{sx}^s \right)^T$ in the equation; then the functional equation is:

$$F(\hat{\mathbf{A}}_x^s) = \hat{\mathbf{A}}_x^s K_x \left(\hat{\mathbf{A}}_x^s \right)^T - 2\hat{\mathbf{A}}_x^s P_x \tag{30}$$

Using the necessary conditions for extrema in the variational principle, we seek the extrema of $F(\hat{\mathbf{A}}_x^s)$ in Equation (30), while ensuring that. Then we obtain:

$$K_x \left(\hat{\mathbf{A}}_x^s \right)^T = P_x \tag{31}$$

We used the same solving method for Equations (17) and (18), and got the final equation as:

$$\begin{cases} K_x(\hat{\mathbf{A}}_x^s)^T = P_x \\ K_y(\hat{\mathbf{A}}_y^s)^T = P_y \\ K_z(\hat{\mathbf{A}}_z^s)^T = P_z \end{cases} \tag{32}$$

where $K_y = \left(\sum_i^N K_{1i} + \sum_i^N K_{2i} + C_{y1} + C_{y2}\right)$, $P_y = \left(\sum_i^N P_{yi}\right)\left(\hat{\mathbf{J}}_{sy}^s\right)^T$, $K_z = (\sum_i^N K_{1i} + \sum_i^N K_{2i} + C_{z1} + C_{z2})$ and $P_z = \left(\sum_i^N P_{zi}\right)\left(\hat{\mathbf{J}}_{sz}^s\right)^T$.

The resulting sparse matrix is shown in Figure 3b. When the finite element method is used to directly solve the three-dimensional partial differential equation, a large matrix must be constructed (e.g., Figure 3a). We use the Fourier transform to convert the three-dimensional problem into multiple mutually independent one-dimensional problems and construct a matrix for each node in the plane. With the aid of parallel computing, matrix construction and solution for all nodes in the horizontal direction can be completed simultaneously. Therefore, under the same mesh size, compared with directly using the finite element method for the solution, our algorithm significantly reduces both the number of matrix elements that need to be stored and the number of unknowns to be solved. Combined with parallel computing, it can substantially improve computational efficiency. Comparing the matrices constructed by the two methods shows that our algorithm only needs to store 5 diagonals, whereas directly using the finite element method to solve the three-dimensional partial differential equation requires storing 63 diagonals. In addition, when LU decomposition is used to solve the matrix, our algorithm requires only approximately 9n floating-point operations, with the forward substitution and back substitution processes requiring approximately 4n operations each. The overall computational complexity is linear O(n) [49,50]. The LU decomposition of a pentadiagonal matrix is essentially a natural extension of the Thomas algorithm (tridiagonal matrix algorithm). Its algorithmic logic is clear, and its banded structure is naturally well suited to vectorization (SIMD) and block parallelism. Therefore, this method combines the high accuracy of direct methods with the linear computational efficiency of banded matrix algorithms.

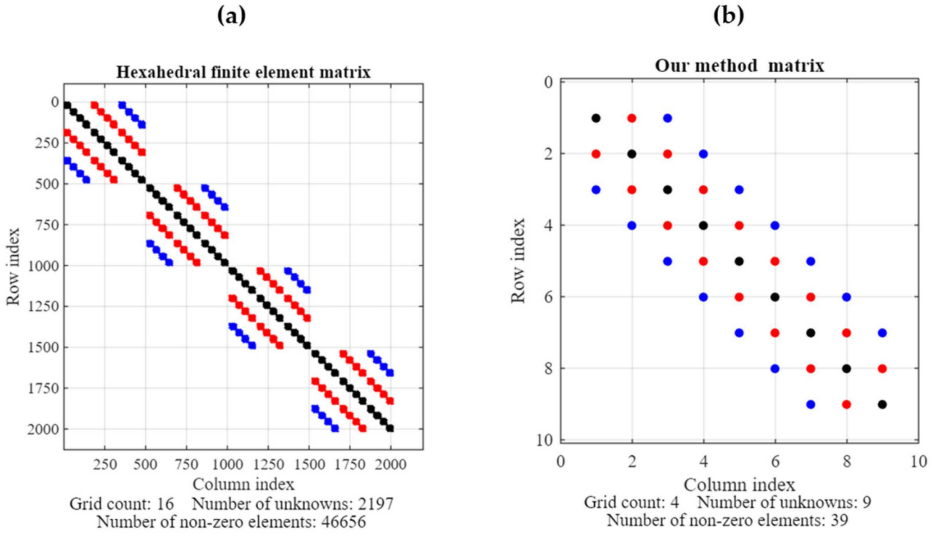


Figure 3. Comparison of finite element matrices for solving equations system. (**a**) Hexahedral finite element matrix, (**b**) Our method finite element matrix. (The three colors correspond to the distributions of the three diagonal elements, respectively.)

2.4. Two-Dimensional Gauss-FFT

In both forward and inverse frequency-domain computations of the standard two-dimensional FFT, the continuous Fourier integral is essentially approximated using the composite rectangular formula. The two-dimensional inverse transform be described as:

$$f(x,y) = \frac{1}{4\pi^2}\iint \psi(k_x,k_y)e^{i(k_x x+k_y y)}dk_x dk_y \tag{33}$$

where k_x and k_y represent the wavenumber in the x and y directions.

We used the Nyquist frequency to discretize Equation (31) and then integrate to obtain:

$$f(x_m,y_N) \approx \frac{\Delta k_x \Delta k_y}{4\pi^2}\sum_{p=-N_x/2}^{N_x/2-1}\sum_{q=-N_y/2}^{N_y/2-1}\psi(p\Delta k_x, q\Delta k_y)e^{i(p\Delta k_x x_m + q\Delta k_y y_N)} \tag{34}$$

where Δk_x and Δk_y represent the sampling interval in the x and y directions, N_x and N_y represent the number of observation points in the x and y directions, p and q represent the discrete sampling point index in the x and y directions.

This approximation involves two types of errors: first, the truncation effect (the spectrum is forced to zero at $|k_x| > K_x$, $|k_y| > K_y$, where K_x and K_y represent the cutoff frequency in the x and y directions); and second, the discretization effect (the algebraic precision of the rectangular formula is only of the zero-order; accuracy decreases significantly when the wave number density is insufficient, and singularities are likely to occur near zero wave numbers).To improve integration accuracy without increasing the total number of sampling points N_x and N_y, the rectangular equation can be replaced with the Gauss-Legendre integration equation in each frequency subinterval, thereby constructing the two-dimensional Gauss-Legendre accelerated Fourier transform (referred to as the two-dimensional Gauss-FFT).

We divide the two-dimensional integration interval [-K_x,K_x] × [-K_y,K_y] into N_x×N_y rectangular subintervals, and then apply a p-point Gauss-Legendre equation along the x-direction and a q-point Gauss-Legendre equation along the y-direction in each subinterval (for simplicity, take p and q of the same order). At the same time, we rewrite the wavenumber as:

$$\begin{aligned} k_x &= \tfrac{\Delta k_x}{2}t + \tfrac{\Delta k_x}{2}(2N+1), T \in [-1,1] \\ k_y &= \tfrac{\Delta k_y}{2}s + \tfrac{\Delta k_y}{2}(2m+1), s \in [-1,1] \end{aligned} \tag{35}$$

Then the integral over the subinterval reduces to:

$$\begin{aligned} &\int_{m\Delta k_y}^{(m+1)\Delta k_y}\int_{n\Delta k_x}^{(n+1)\Delta k_x}\psi(k_x,k_y)e^{i(k_x x+k_y y)}dk_x dk_y \\ &\approx \frac{\Delta k_x \Delta k_y}{4}\sum_{a=0}^{p-1}\sum_{b=0}^{p-1}A_a^p B_b^p \psi\left(\frac{\Delta k_x}{2}t_a + \frac{\Delta k_x}{2}(2n+1), \frac{\Delta k_y}{2}s_b + \frac{\Delta k_y}{2}(2m+1)\right) \\ &\times e^{i[(\frac{\Delta k_x}{2}t_a + \frac{\Delta k_x}{2}(2n+1))x + (\frac{\Delta k_y}{2}s_b + \frac{\Delta k_y}{2}(2m+1))y]} \end{aligned} \tag{36}$$

where t_a and s_b represent the zeros of the pth-order Legendre polynomials, and A_a^p, B_b^p represent the corresponding integration coefficients. The shift wavenumber is defined as:

$$\begin{aligned} k_x^{(a)}(n) &= \left[n + \tfrac{t_a+1}{2}\right]\Delta k_x,\ a = 0,\ldots,p-1 \\ k_y^{(b)}(m) &= \left[m + \tfrac{s_b+1}{2}\right]\Delta k_y,\ b = 0,\ldots,p-1 \end{aligned} \tag{37}$$

Then the two-dimensional Gauss-Legendre inverse transform can be written as:

$$f(x_m,y_n) = \frac{1}{4\pi^2}\sum_{a=0}^{p-1}\sum_{b=0}^{p-1}\frac{A_a^p B_b^p}{4}\sum_{n=-N_x/2}^{N_x/2-1}\sum_{m=-N_y/2}^{N_y/2-1}\psi(k_x^{(a)}(n),k_y^{(b)}(m))e^{i(k_x^{(a)}(n)x_m + k_y^{(b)}(m)y_n)}\Delta k_x \Delta k_y \tag{38}$$

Noted that the phase factor can be decomposed as:

$$e^{i(k_x^{(a)}(n)x_m+k_y^{(b)}(m)y_n)} = e^{i(n\Delta k_x x_m+m\Delta k_y y_n)}e^{i(\Delta k_x \frac{t_a+1}{2}x_m+\Delta k_y \frac{s_b+1}{2}y_n)} \tag{39}$$

where the first term is precisely the kernel of the standard two-dimensional IFFT. Therefore, Equation (38) can be rearranged as:

$$f(x_m,y_n) = \sum_{a=0}^{p-1}\sum_{b=0}^{p-1}\frac{A_a^p B_b^p}{4} IFFT2\left[\psi(k_x^{(a)},k_y^{(b)})\right]e^{i(\Delta k_x \frac{t_a+1}{2}x_m+\Delta k_y \frac{s_b+1}{2}y_n)} \tag{40}$$

The calculation procedure is as follows:

(1) We looked it up in the table to get the Gaussian nodes at point p, the zeros of the pth-order Legendre polynomials (t_a and s_b), along with the coefficients (A_a^p and B_b^p);

(2) For each set ($\mathbf{a}$,b), we obtain the spectral values ψ on the offset w-grid $\left(k_x^{(a)}(n),\ k_y^{(b)}(m)\right)$ (these can be calculated directly from the theoretical spectrum or interpolated from an existing discrete spectrum);

(3) We obtain the matrix $IFFT2_{ab}[m,n]$ by invoking the standard two-dimensional IFFT;

(4) Finally, We multiply the matrix by the phase factor ($e^{i(\Delta k_x(t_a+1)x_m/2+\Delta k_y(s_b+1)y_n/2)}$) and weight coefficients ($A_a^p B_b^p/4$), and then sum over all intervals to obtain the frequency domain $f(x_m,y_n)$ of $f(x,y)$.

This method maintains the FFT's $O(N_xN_y log(N_xN_y))$ computational complexity, adding only a constant factor of p^2 to the computational load, while increasing the algebraic precision from order 0 to order $2p-1$.As shown in Figure 4, which presents a logarithmic plot of the errors between the results of the standard Fourier transform and the Gauss-FFT and the exact results for the same grid and sampling rate, it can be seen that the error in the Gauss-FFT results is far smaller than that of the standard Fourier transform, and the error gradually decreases as the number of higher-order nodes increases.

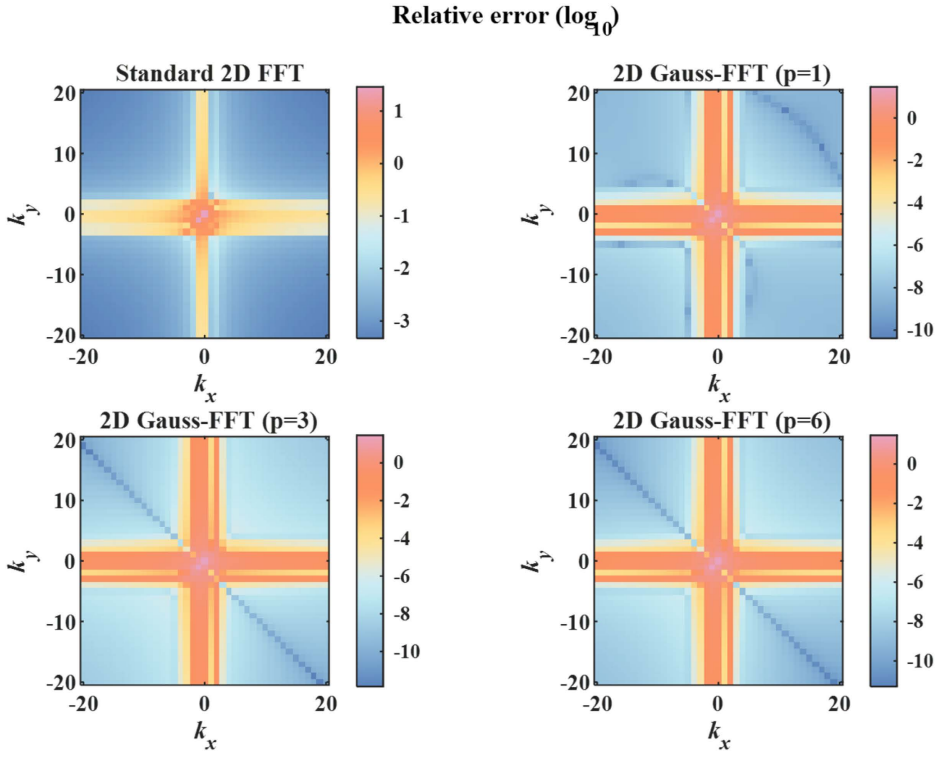


Figure 4. Comparison of errors between the standard FFT and Gauss-FFT with different nodes.

The two-dimensional forward transform is defined by:

$$F(k_x, k_y) = \iint f(x,y)e^{-i(k_x x + k_y y)}dxdy \tag{41}$$

Similarly, the p-point Gauss-Legendre forward transform equation is then given by:

$$F(k_x^{(a)}, k_y^{(b)}) = FFT2[f(x,y)]e^{-i(\Delta k_x \frac{t_a+1}{2} x_1 + \Delta k_y \frac{s_b+1}{2} y_1)}e^{-i(k_x^p x_1 + k_y^q y_1)} \tag{42}$$

where $k_x^p = p\Delta k_x$ and $k_y^q = q\Delta k_y$ represent the standard discrete wavenumber. In actual programming, the constant phase factor can be pre-incorporated into the FFT input array, and the calculation can be performed using a standard 2D FFT library.

2.5. Algorithm Flow

(1) Dimension Reduction of the Computational Domain and Grid Discretization: In the horizontal directions (x, y), uniform division is adopted, while in the vertical direction (z), uniform or non-uniform division can be chosen depending on the complexity of the geological structure, to construct a three-dimensional grid system. Based on the sampling theorem, the discrete range of horizontal wavenumbers k_x and k_y are determined. Subsequently, a two-dimensional Fourier transform is applied to the spatial domain control equations, reducing the three-dimensional partial differential problem to a series of one-dimensional frequency-domain problems.

(2) Define model parameters: The physical properties of the subsurface medium—including electrical conductivity, magnetic permeability, and dielectric permittivity—are assigned at the grid nodes. The corresponding anomalous conductivity distribution is then calculated for the prescribed frequency parameters.

(3) Initialization of the background field and separation of the anomalous response: The electromagnetic field distribution in the background medium, without anomalous bodies, is first calculated and used as the initial estimate for the iterative solution. An anomalous conductivity tensor is subsequently introduced. Based on the total electric field obtained from the preceding iteration, the scattering current density induced by medium polarization is approximated. This procedure provides an initial separation of the secondary-field response associated with the anomalous body.

(4) Solution of the secondary field in the wave-number domain and field reconstruction: The calculated scattered current density is mapped back to the wave-number domain, substituted into the electromagnetic field integral equations, and combined with boundary conditions to solve for the secondary vector potential at each discrete wavenumber point. The relationship between the secondary field vector potential in the maxed space-wavenumber domain and the secondary electromagnetic field is given by Equations (45) and (46). The quadratic electric field in the horizontal wave number domain is inverted back to physical space via an inverse Fourier transform, then superimposed on the background field to form the total electric field estimate for the current iteration step.

$$\begin{cases} \mathbf{E}_x^s = -i\mu\omega\hat{\mathbf{A}}_x^s + \frac{1}{\sigma_b + i\mu\omega} ik_x \left(ik_x\hat{\mathbf{A}}_x^s + ik_y\hat{\mathbf{A}}_y^s + \frac{\partial\hat{\mathbf{A}}_z^s}{\partial z} \right) \\ \mathbf{E}_y^s = -i\mu\omega\hat{\mathbf{A}}_y^s + \frac{1}{\sigma_b + i\mu\omega} ik_y \left(ik_x\hat{\mathbf{A}}_x^s + ik_y\hat{\mathbf{A}}_y^s + \frac{\partial\hat{\mathbf{A}}_z^s}{\partial z} \right) \\ \mathbf{E}_z^s = -i\mu\omega\hat{\mathbf{A}}_z^s + \frac{1}{\sigma_b + i\mu\omega} \frac{\partial}{\partial z} \left(ik_x\hat{\mathbf{A}}_x^s + ik_y\hat{\mathbf{A}}_y^s + \frac{\partial\hat{\mathbf{A}}_z^s}{\partial z} \right) \end{cases} \tag{43}$$

$$\begin{cases} \mathbf{H}_x^s = ik_y\hat{\mathbf{A}}_z^s - \frac{\partial\hat{\mathbf{A}}_y^s}{\partial z} \\ \mathbf{H}_y^s = \frac{\partial\hat{\mathbf{A}}_x^s}{\partial z} - ik_x\hat{\mathbf{A}}_z^s \\ \mathbf{H}_z^s = ik_x\hat{\mathbf{A}}_y^s - ik_y\hat{\mathbf{A}}_x^s \end{cases} \tag{44}$$

To improve the accuracy of the numerical solution, the electric field values at three equidistant nodes near the ground surface can be used to calculate the partial derivatives, in which case we have:

$$\left.\frac{\partial \hat{\mathbf{A}}_z^s}{\partial z}\right|_{z=0} = \frac{1}{L}\left(-3\hat{\mathbf{A}}_{1z}^s + 4\hat{\mathbf{A}}_{2z}^s - \hat{\mathbf{A}}_{3z}^s\right) \tag{45}$$

where L denotes the length of the solution cell, $\hat{\mathbf{A}}_{1z}^s$, $\hat{\mathbf{A}}_{2z}^s$ and $\hat{\mathbf{A}}_{3z}^s$ represent the values of the quadratic field vector components in the mixed space-wavenumber domain at the start, middle, and end nodes of the solution cell.

(5) Iterative Convergence Criterion and Magnetic Field Calculation: Within the electromagnetic integral-equation framework, the nonlinear coupling between the electric-field vector and the anomalous scattering current density is evaluated. In this study, a contraction-operator scheme is employed to construct a stable iterative formulation. Convergence is assessed by monitoring the difference between the field values obtained at two successive iterations, as expressed in Equations (46) and (47). If the prescribed convergence criterion is not satisfied, the updated electric field is used to recalculate the scattering current density, and the iteration is continued. Once the convergence condition in Equation (48) is satisfied, the secondary magnetic field is calculated in the wavenumber domain under the Lorenz gauge. After inverse transformation and superposition with the background magnetic field, the complete three-dimensional electromagnetic-field distribution throughout the computational domain is obtained.

$$\mathbf{E}^{(n)} = \alpha\mathbf{E}^{(n)} + \beta\mathbf{E}^{(n-1)} \tag{46}$$

Here, $\mathbf{E}^{(n-1)}$ represents the total electric field corrected by the tightening operator from the previous iteration step, and $\mathbf{E}^{(n)}$ represents the current forward-calculation estimate. The corresponding convergence coefficient is defined as:

$$\begin{cases} \alpha = \frac{2\sigma_b}{2\sigma_b+\sigma_s} \\ \beta = \frac{\sigma_s}{2\sigma_b+\sigma_s} \end{cases} \tag{47}$$

$$\varepsilon\left\{\mathbf{E}^{(n+1)}, \mathbf{E}^{(n)}\right\} = \frac{\sum\left|\mathbf{E}^{(n+1)}\right| - \sum\left|\mathbf{E}^{(n)}\right|}{\sum\left|\mathbf{E}^{(n+1)}\right|} < 10^{-4}, or\ n > 40 (n : iteration\ count) \tag{48}$$

For the implementation process, see Figure 5.

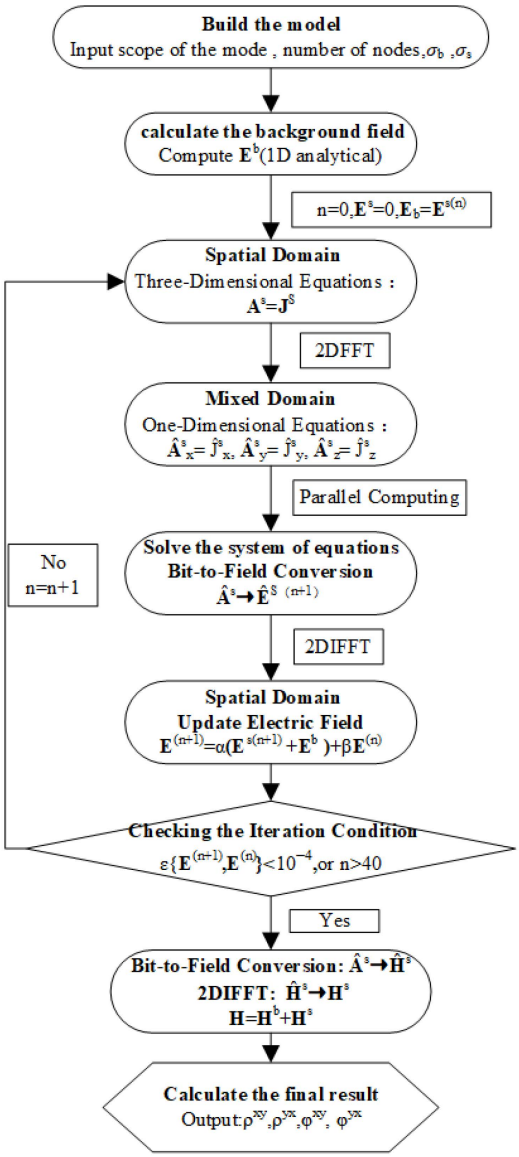


Figure 5. Flowchart of 3D magnetotelluric forward modeling algorithm.

3. Numerical Examples

3.1. Validation of the COMMEMIM 3D-1 Model

First, we used the widely adopted COMMEMI 3D-1 model developed by Zhdanov et al. to evaluate the numerical performance of the proposed algorithm [51]. The COMMEMI 3D-1 model consists of an upright prismatic anomaly located in a homogeneous half-space with a resistivity of 100 Ω·m and an air conductivity of 10^{-12} Ω·m. The computational domain is 2.5 × 2.5 × 2.5 km^3, with a horizontal range of −2.5 km to 2.5 km in the x-direction; −2.5 km to 2.5 km in the y-direction; and 0 to 2.5 km in the z-direction. Directly below the origin lies a prismatic anomaly with dimensions of 1.0 × 2.0 × 2.0 km^3, a top surface depth of 0.25 km, and a resistivity of 0.5 Ω·m. The resistivity ratio is $\rho^b/\rho^s = 200$(where ρ^b represents the resistivity of the uniform half-space and ρ^s represent the resistivity of the anomaly), as shown in Figure 6. These results are indicative of the algorithm's convergence and correct verification. The mesh has 201 × 201 × 201 nodes, with uniform meshing in all three directions; the sampling intervals are 25 m in the x and y directions and 12.5 m in the z-direction; the Gauss-Legendre quadrature orders are p = q = 3, the horizontal wavenumber range follows the sampling theorem, $N_x = N_y = 201$ and $\Delta k_x = \Delta k_y \approx 1.25 \times$

10^{-3} rad/m; the anomaly body extends over a 10 × 20 × 90 region; and the calculations were performed at frequencies of 10 Hz and 0.1 Hz.

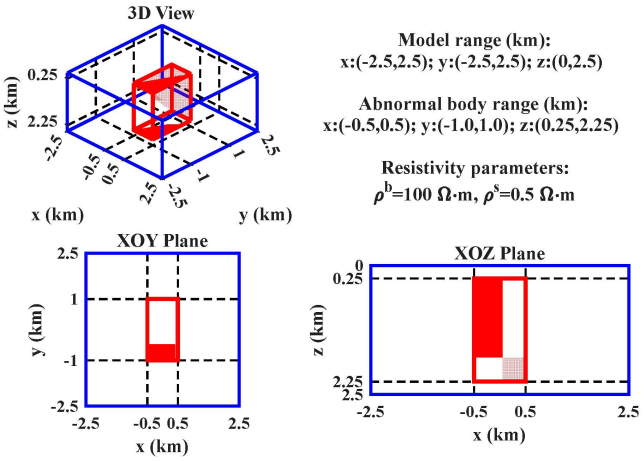


Figure 6. 3D and cross-section diagram of COMMEMI 3D-1 low-resistance prism geoelectric model.

The comparison between the computational results of the algorithm proposed in this paper and the COMMEMI 3D-1 reference values is shown in Figures 7 and 8. Overall, the computational results agree well with the benchmark responses of COMMEMI 3D-1, verifying the correctness of the spatial-wavenumber hybrid-domain algorithm.

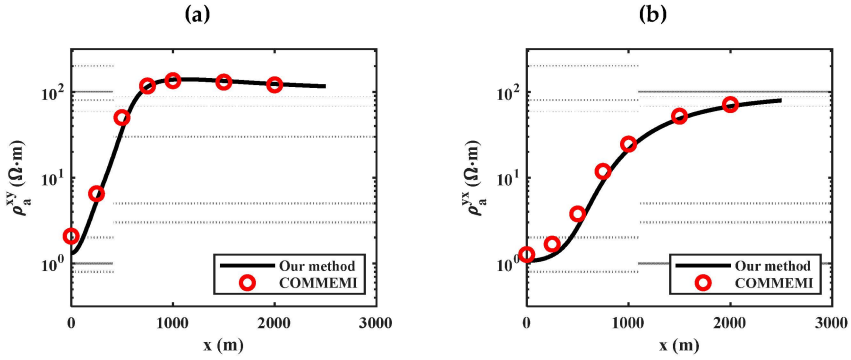


Figure 7. Comparison of apparent resistivity ρ^{xy} and ρ^{yx} response curves between the proposed algorithm and standard model at 0.1 Hz. (**a**) ρ^{xy} comparison of results, (**b**) ρ^{yx} comparison of results.

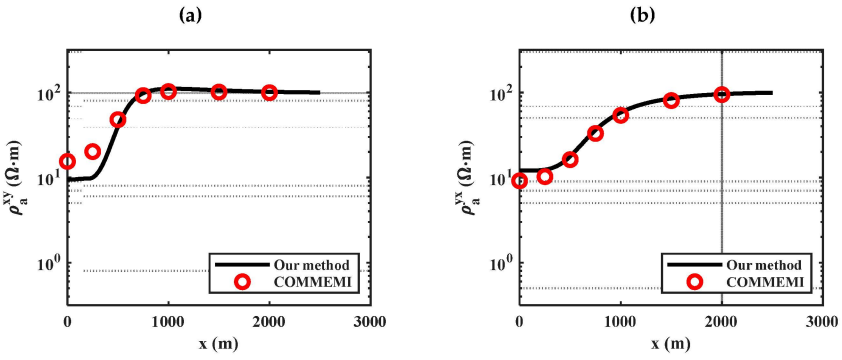


Figure 8. Comparison of apparent resistivity ρ^{xy} and ρ^{yx} response curves between the proposed algorithm and standard model at 10 Hz. (**a**). ρ^{xy} comparison of results, (**b**). ρ^{yx} comparison of results.

The results at $f = 0.1$ Hz (e.g., Figure 7) reflect the resistivity response curve at the center of the anomalous body. Compared with the COMMEMI 3D-1 reference values, the resistivity

response obtained by the proposed algorithm near the center of the anomalous body is closer to the resistivity of the anomalous body itself. At the boundary of the anomalous body, however, its spurious extremum is significantly smaller than the COMMEMI 3D-1 reference value and is closer to the response of a homogeneous half-space.

The results at $f = 10$ Hz (e.g., Figure 8) reflect the resistivity response curve at the upper boundary of the anomalous body. In this region, the resistivity response obtained by the proposed algorithm is closer to the response of a homogeneous half-space than the COMMEMI 3D-1 reference value.

To verify the reliability of the algorithm, plane contour maps at the ground surface were plotted, based on which the extent of the anomalous body was delineated. Analysis of Figures 9 and 10 shows that the surface apparent resistivity contour maps obtained using the proposed algorithm are generally consistent with the actual morphology of the anomalous body, thereby verifying the correctness of the algorithm.

A further comparison of Figure 9a,b and Figure 10a,b reveals that the anomalous response of ρ^{xy} is significantly stronger than that of ρ^{yx}. This is because when the polarization current propagates along the x direction, the anomalous body can be approximately regarded as extending along the y direction. Its extent in the y direction is greater than that in the x direction, and therefore the anomalous response of ρ^{xy} is much stronger than that of ρ^{yx}. Consequently, ρ^{xy} can characterize the morphology of the anomalous body more clearly.

In addition, because our method adopts a vector-potential-based solution method and introduces a divergence-correction condition at the boundary of the anomalous body, the anomalous morphology obtained at 10 Hz (e.g., Figure 10) is clearly superior to that obtained at 0.1 Hz (e.g., Figure 10).

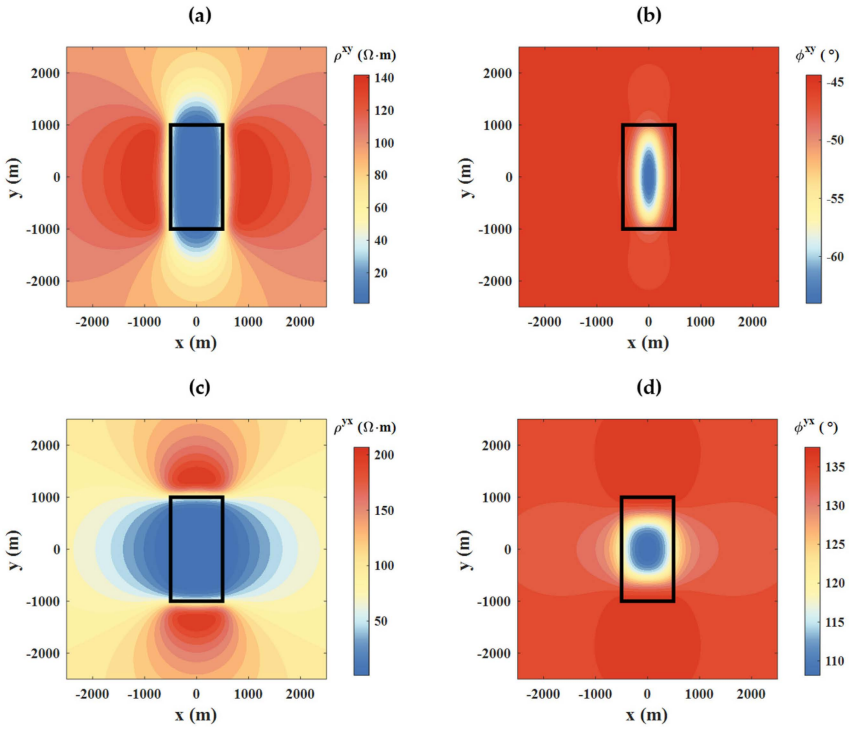


Figure 9. Contour maps of surface apparent resistivity and phase at 0.1 Hz. (**a**) ρ^{xy} result, (**b**) φ^{xy} result, (**c**) ρ^{yx} result, (**d**) φ^{yx} result.

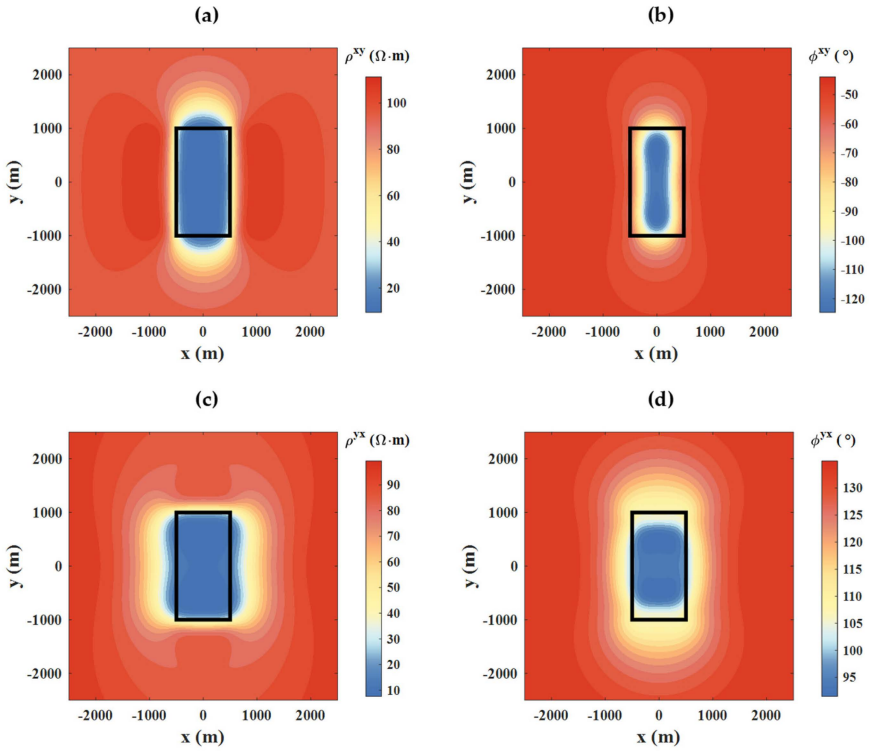


Figure 10. Contour maps of surface apparent resistivity and phase at 10 Hz. (**a**) ρ^{xy} result, (**b**) φ^{xy} result, (**c**) ρ^{yx} result, (**d**) φ^{yx} result.

3.2. Validation of the Low-Resistivity Thin-Plate Model

We constructed a low-resistivity plate (e.g., Figure 11) to verify the accuracy of the algorithm results. The model computational domain is $2 \times 2 \times 1$ km^3, with the horizontal x and y ranges both being -1 to 1 km and the vertical z range being 0 to 1 km. A low-resistivity thin-plate anomaly body is placed directly below the origin, with dimensions of $0.8 \times 0.8 \times 0.2$ km^3, a top depth of 0.2 km, and a resistivity of 10 Ω·m. The model has $201 \times 201 \times 201$ grid nodes, with uniform discretization in all three directions, the Gauss-Legendre quadrature orders are p = q = 3, the horizontal wavenumber range follows the sampling theorem, $\Delta x = \Delta y = 10$ m, $N_x = N_y = 201$ and $\Delta k_x = \Delta k_y \approx 3.13 \times 10^{-3}$ rad/m; The sampling intervals in the x and y directions are both 10 m, and that in the z direction is 5 m; the cell range corresponding to the anomaly body is $40 \times 40 \times 20$. The computational frequencies are 1000 Hz, 100 Hz, 10 Hz, 1 Hz, and 0.1 Hz.

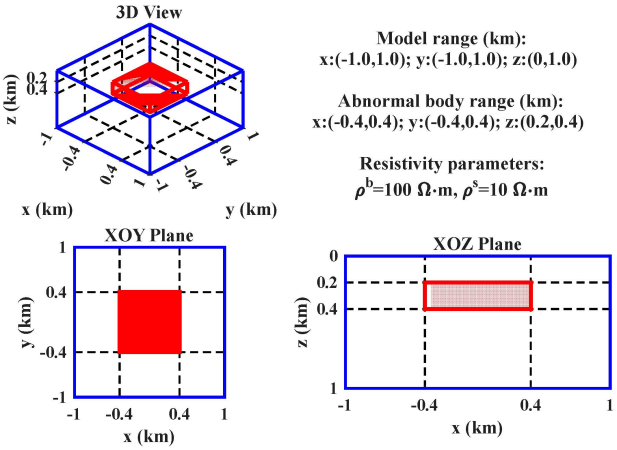


Figure 11. Spatial and cross-section structure of 3D low-resistance thin-sheet geoelectric model.

Analysis of the three-dimensional slice plots (e.g., Figure 12) indicates that the high-frequency portion mainly reflects shallow information, with both resistivity and phase exhibiting the characteristics of a uniform half-space. A distinct low-resistivity anomaly appears in the intermediate-frequency portion, where the anomaly reaches its minimum value. As the frequency decreases further, the anomaly gradually weakens, and the phase progressively returns to the response of a uniform half-space. The spatial distribution locations of the resistivity and phase anomalies are basically consistent. Their variation with frequency agrees with the theory of electromagnetic-field propagation and closely matches the range of the anomaly body in the constructed model, thereby verifying the reliability of the algorithm.

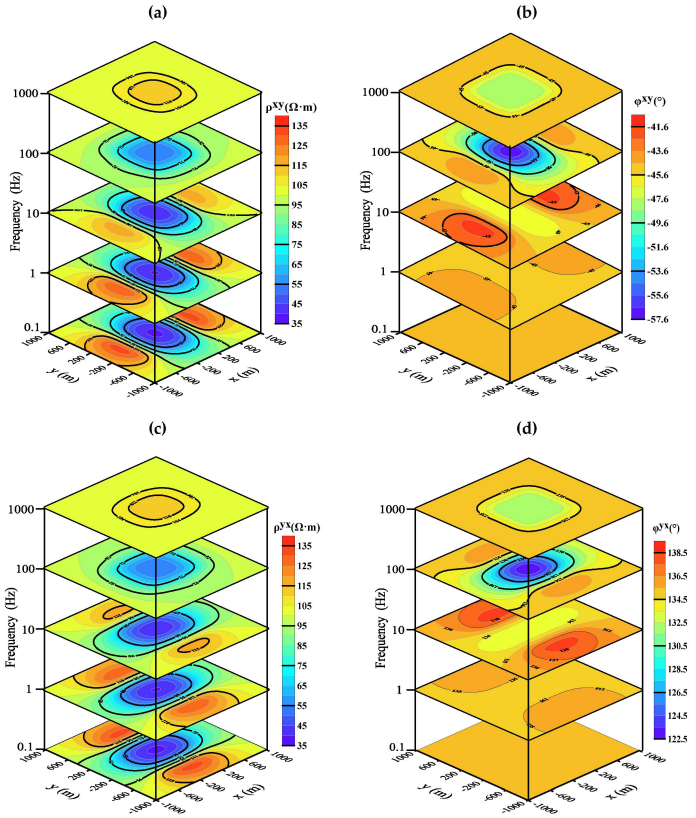


Figure 12. Multi-layer contour slices of resistivity and phase for low-resistance model at multiple frequencies. (**a**). ρ^{xy} result, (**b**). φ^{xy} result, (**c**). ρ^{yx} result, (**d**). φ^{yx} result.

To verify the accuracy after introducing the divergence condition, the 10 Hz calculation results were compared with those obtained using the open-source software SimPEG (version 0.18.0). SimPEG is a classic software package that uses the finite-volume method (MFV) to solve three-dimensional magnetotelluric forward problems [52,53]. It employs a total-field and background-field decomposition strategy, offering the advantages of a smaller numerical dynamic range and more stable calculation results. In addition, its boundary conditions can be automatically satisfied by the analytical conditions of the background field at infinity. The model constructed in SimPEG has a horizontal extent of −75,793.33~75,793.33 m in the x direction and −75,793.33~75,793.33 m in the y direction, while the computational range in the z direction is −75,793.33~11,186.58 m, with a total of 58,080 grid cells.

Without considering the divergence condition (e.g., Figure 13), the results of the algorithm exhibit relatively large errors near the boundaries of the anomalous body compared with the SimPEG results. The maximum relative errors in resistivity and phase are 7.85% and 3.58%, respectively, failing to meet the accuracy requirements for forward modeling. Therefore, our algorithm introduces a divergence condition so that the discrete cells con-

tinue to satisfy the divergence condition at the boundaries, thereby effectively reducing errors caused by abrupt resistivity changes. As shown in Figure 14, after incorporating the divergence condition, the errors near the anomalous body are significantly reduced. The maximum relative errors in resistivity and phase are 3.92% and 0.60%, respectively, meeting the accuracy requirements for forward modeling.

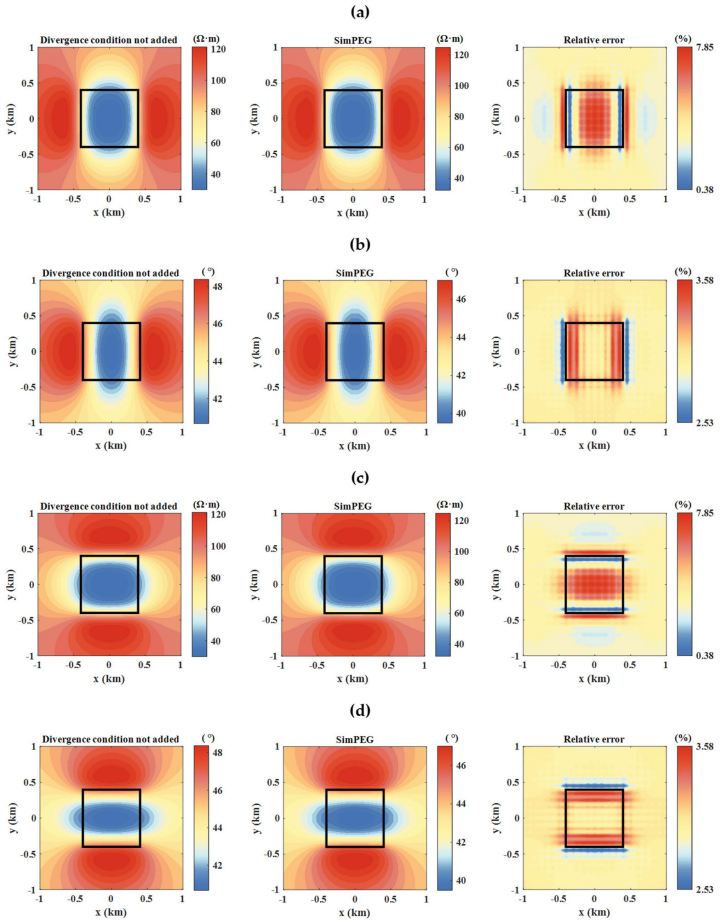


Figure 13. Plane comparison of resistivity, phase and relative error between Algorithm before adding divergence condition and SimPEG at 10 Hz. (**a**) ρ^{xy} error results without adding divergence condition, (**b**) φ^{xy} error results without adding divergence condition, (**c**) ρ^{yx} error results without adding divergence condition, (**d**) φ^{yx} error results without adding divergence condition.

A comparison of the planar contour plots generated by the algorithm proposed in this paper and the MFV method shows that certain errors still exist in the uniform half-space region for both methods. To analyze the sources of these errors, response curves of resistivity and phase varying with y were plotted at $x = 0$, 0.4 and 1 km, respectively, as shown in Figure 15. The results indicate that the calculated results of the proposed algorithm and the MFV method are relatively close at the center of the anomalous body ($x = 0$ km) and at its edge ($x = 0.4$ km). At the boundary far from the anomalous body ($x = 1$ km), however, the resistivity obtained by the proposed algorithm is closer to the theoretical value for a uniform half-space.

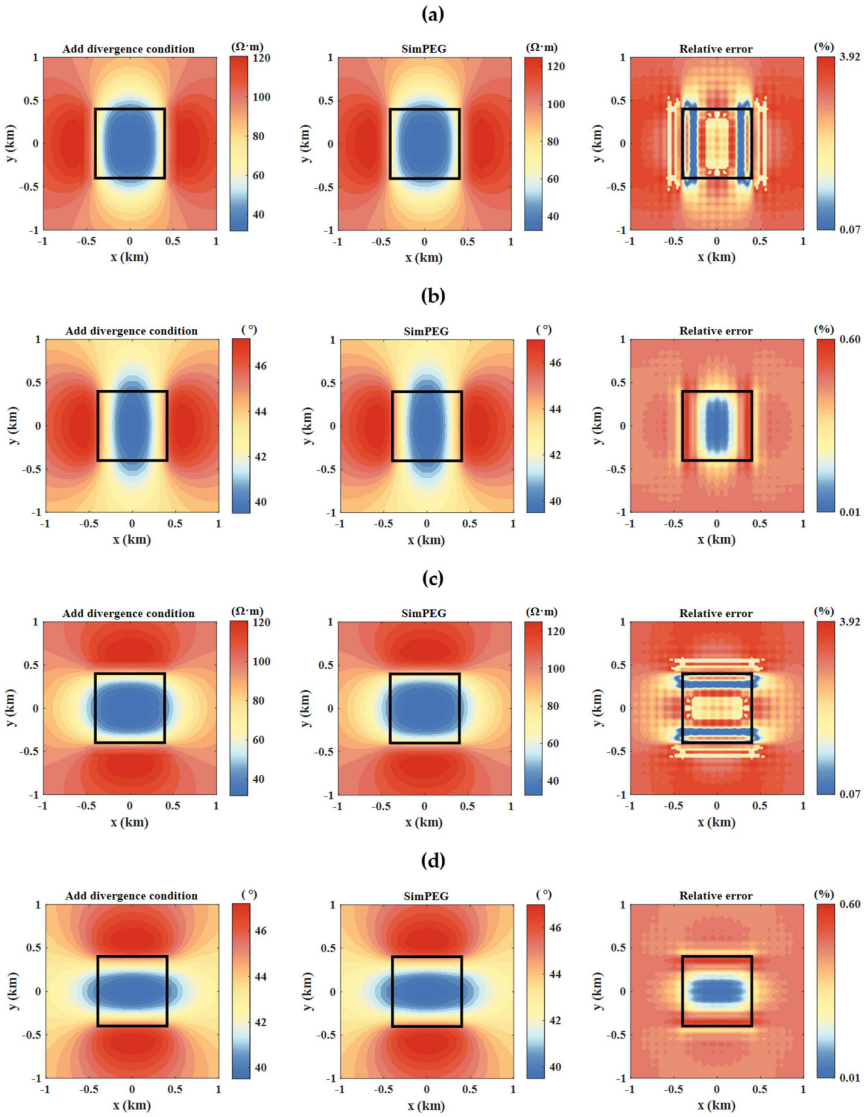


Figure 14. Plane comparison of resistivity, phase and relative error between Algorithm after adding divergence condition and SimPEG at 10 Hz. (**a**) ρ^{xy} error added divergence condition, (**b**). φ^{xy} error added divergence condition, (**c**) ρ^{yx} error added divergence condition, (**d**) φ^{yx} error added divergence condition.

The finite-volume method in SimPEG generally requires the computational domain to be extended sufficiently so that the boundaries are far from the anomalous body, thereby ensuring that the far-field approximation condition is satisfied at the boundaries. In addition, nonphysical reflections generated by the artificially truncated boundaries can affect the interior field domain. Our algorithm decomposes electromagnetic-wave propagation in the subsurface into upward- and downward-propagating waves and removes the boundary-reflected waves. Therefore, it can effectively suppress the influence of nonphysical reflections caused by artificially truncated boundaries on the interior field domain without requiring the boundaries to be placed excessively far away. While reducing the model extent, it can also provide refined discretization of the uniform half-space region. It can thus be seen that the proposed algorithm can satisfy the far-field condition without extending the computational boundaries over a large range, thereby making the background field closer to the model resistivity. Furthermore, by introducing the divergence condition, the errors generated at the boundary of the anomalous body can be further reduced effectively.

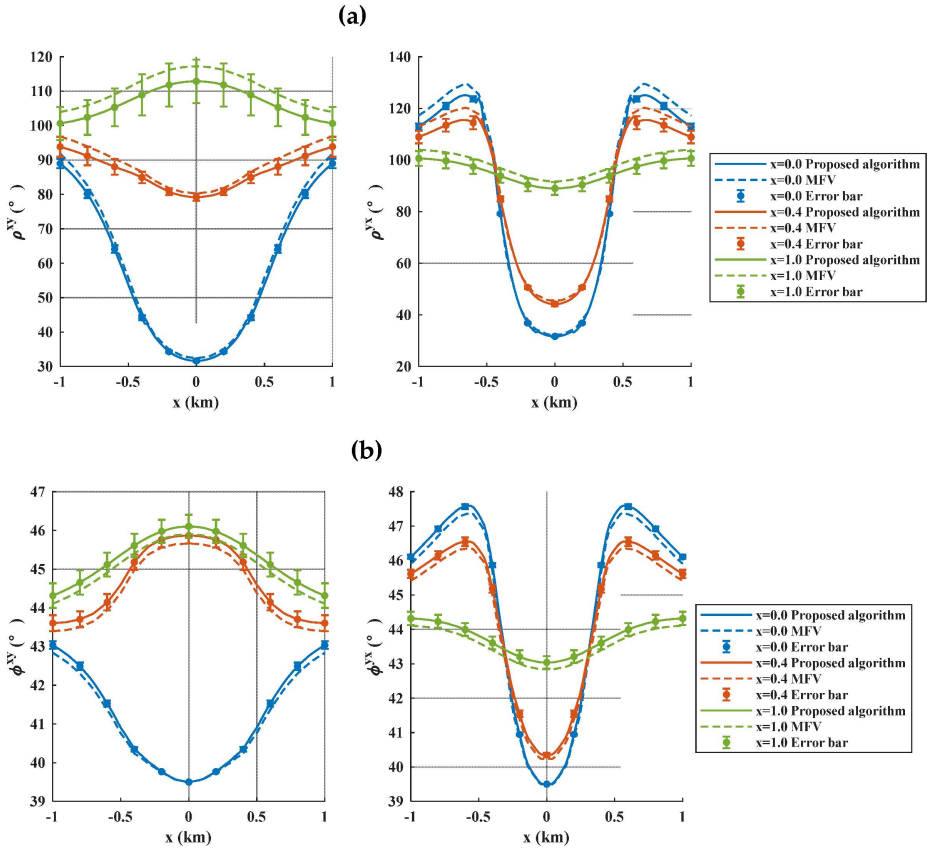


Figure 15. Error curve comparison of resistivity and phase responses along different survey lines of low-resistance model. (**a**) Comparison of resistivity results, (**b**) Comparison of phase results.

3.3. Validation of the High-Resistivity Block Model

To verify the computational efficiency of our algorithm, a high-resistivity block model was constructed, as shown in Figure 16. The model covers a computational domain of $2 \times 2 \times 1$ km^3, with horizontal ranges of -1 to 1 km in the x direction and -1 to 1 km in the y direction; the vertical (z direction) computational range is 0 to 1 km, the Gauss-Legendre quadrature orders are p = q = 3, the horizontal spacings are $\Delta x = \Delta y = 40$ m, 20 m, and 10 m for the 51×51, 101×101 and 201×201 grids, respectively, with corresponding $K_x = K_y = \pi/\Delta x$. A high-resistivity cubic anomaly was placed directly below the origin. It has dimensions of $0.4 \times 0.4 \times 0.4$ km^3, a top depth of 0.4 km, and a resistivity of 1000 Ω·m. The computational frequency was set to 10 Hz, and uniform grids were used in all three directions.

The computational efficiency of the algorithm was recorded by varying the number of grid nodes. Because the iteration time for each layer is affected by the operating state of the computer, the number of iterations was set to 40, and the average time per iteration was calculated. All computations were performed on a workstation equipped with an 11th Gen Intel(R) Core(TM) i7-11800H CPU (8 cores/16 logical processors, 2.30 GHz) and 16 GB RAM (2 × 8 GB DDR4 3200 MHz, Micron), running Windows 11 Home (64-bit). The proposed algorithm was implemented in MATLAB R2021a (9.10.0.1602886). The MATLAB thread setting was fixed at maxNumCompThreads = 6 (utilizing 6 logical cores with hyper-threading enabled), with Intel MKL 2019.0.3 and LAPACK 3.7.0 providing the underlying linear algebra routines. The built-in PARDISO sparse solver was used. For comparison, COMSOL Multiphysics 6.3 was run using its default MUMPS/PARDISO solver with 8 threads. To ensure reproducibility, "time per iteration" refers to the averaged time of one forward/iteration step, whereas "total forward time" refers to the complete forward

modeling (40 iterations unless otherwise stated). The results are presented in Table 1; the curves showing the variation in single-iteration time and memory usage with the number of computational nodes are shown in Figure 17.

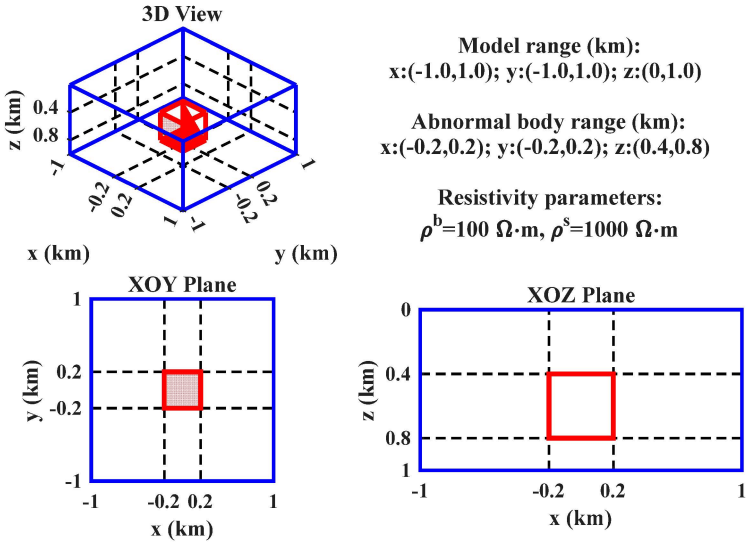


Figure 16. Geometric schematic of 3D high-resistance cubic geoelectric model.

Table 1. Statistical comparison of forward modeling accuracy errors for 3D magnetotelluric methods with different numerical algorithms.

Grid Nodes	Computing Nodes	Abnormal Body Meshes	Time per Iteration (s)	Total Forward Time (s)	Memory (MB)
51 × 51 × 51	132,651	5 × 5 × 5	0.102	4.08	115.6
101 × 101 × 51	520,251	10 × 10 × 5	0.461	18.44	457.2
101 × 101 × 101	1,030,301	10 × 10 × 10	1.045	41.80	1126.4
201 × 201 × 101	4,080,501	20 × 20 × 10	3.928	157.12	3956.3
201 × 201 × 201	8,120,601	20 × 20 × 20	8.707	348.28	8728.1

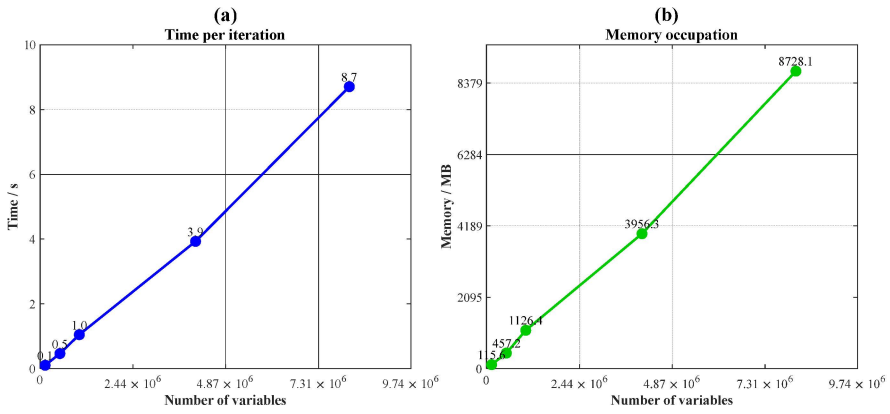


Figure 17. Curves of the average time per iteration and memory consumption versus the number of grid nodes. (**a**) Calculate a graph of the relationship between time per iteration and number of nodes, (**b**) Plot a graph showing the relationship between memory per iteration and number of nodes.

It can be seen from the figures and tables that both the single-iteration time and memory usage of our algorithm increase linearly with the number of computational nodes, demonstrating good computational performance. For a model containing 500,000 nodes,

a single forward calculation takes approximately 0.5 s and uses approximately 460 MB of memory; for a model containing 4 million nodes, a single forward calculation takes approximately 4 s and uses approximately 4 GB of memory. Overall, the algorithm has a fast computational speed, low memory usage, and high computational efficiency.

Furthermore, to examine the effect of the number of anomalous bodies on iteration time and memory consumption, four anomalous bodies were embedded in the 201 × 201 × 201 mesh listed in Table 1. The anomalous model is shown in Figure 18: bodies 1 and 4 are low-resistivity prisms of 10 Ω·m, whereas bodies 2 and 3 are high-resistivity prisms of 1000 Ω·m. The forward responses at 100 Hz are presented in Figure 19. With the iteration count fixed at the same value, repeated experiments show that the number of anomalous bodies has no effect on iteration time—the time for multiple bodies remains identical to that for a single body—while the memory consumption of the four-body model is doubled relative to that of the single-body model.

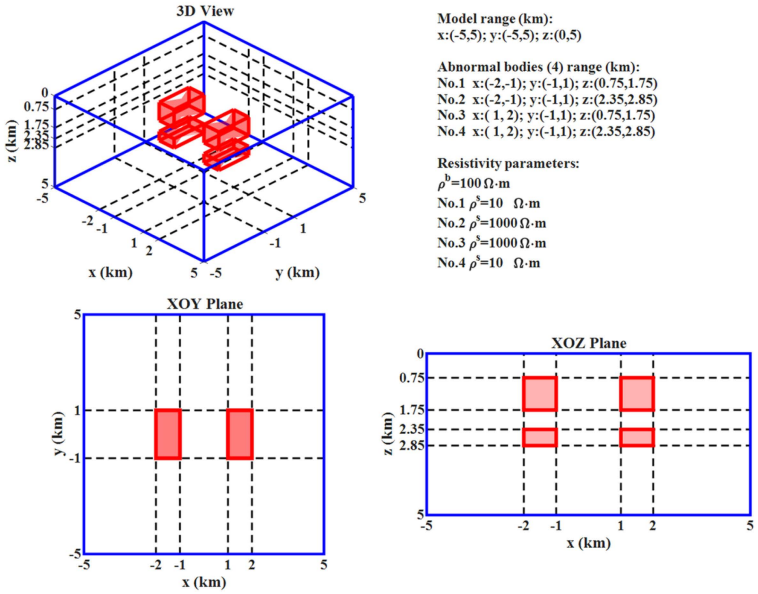


Figure 18. Geometric schematic of the combined geoelectric model with high-resistivity and low-resistivity prisms.

To verify both the computational efficiency and accuracy of the proposed algorithm, we employed the commercial finite-element software Comsol Multiphysics 6.3 to simulate the same model. Comsol's MT forward solver adopts a three-dimensional vector finite-element formulation based on tetrahedral elements on an unstructured mesh, with local refinement applied near the anomalous bodies and the air–Earth interface. This formulation avoids the staircase errors inherent in structured meshes as well as the spurious modes associated with nodal finite-element methods. By progressively varying the mesh resolution, we compared the computation time and memory usage of the two approaches, as summarized in Table 2. Both quantities increase sharply as the Comsol mesh is refined. The final mesh (Figure 20) was obtained by successively refining the elements until the relative error in the surface apparent resistivity fell below 3%. With this fine mesh, the maximum relative errors in apparent resistivity and phase are 2.53% and 0.10%, respectively (Figure 21). These results demonstrate that the proposed algorithm achieves high computational efficiency for large-scale forward modeling while maintaining the required accuracy.

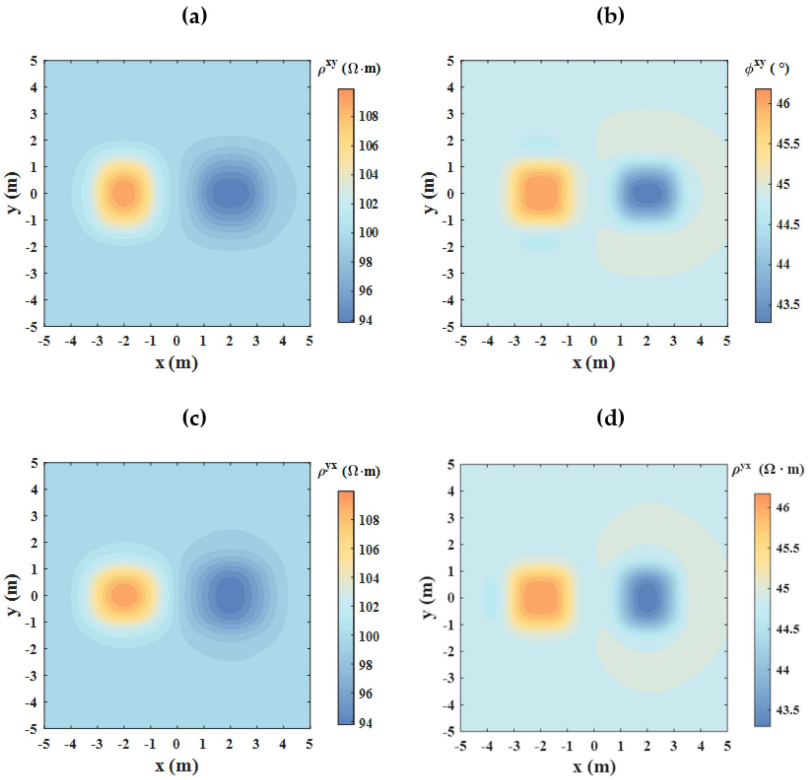


Figure 19. Contour maps of resistivity and phase for the combined model at 100 Hz. (**a**). ρ^{xy} result, (**b**). φ^{xy} result, (**c**). ρ^{yx} result, (**d**). φ^{yx} result.

Table 2. Statistics of the total forward time and memory consumption of the proposed algorithm and Comsol under different grid scales.

Methed	Cell Size	Number of Elements	Solve for Degrees of Freedom	Total Forward Time (s)	Memory (GB)
Comsol	Large cell	30,500	198,980	14	3.15
	Medium cell	120,625	778,128	51	6.23
	Small cell	662,278	4,235,672	378	25.56
Our method	Large cell	31,250	125,000	4.2	0.31
	Medium cell	132,651	530,604	19	1.59
	Small cell	1,030,301	4,121,204	42	6.24

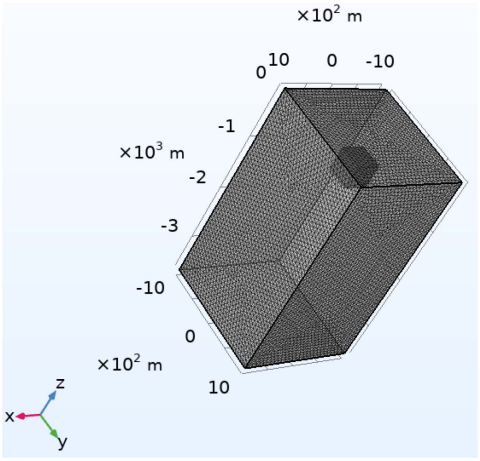


Figure 20. Schematic diagram of the unstructured mesh used in Comsol.

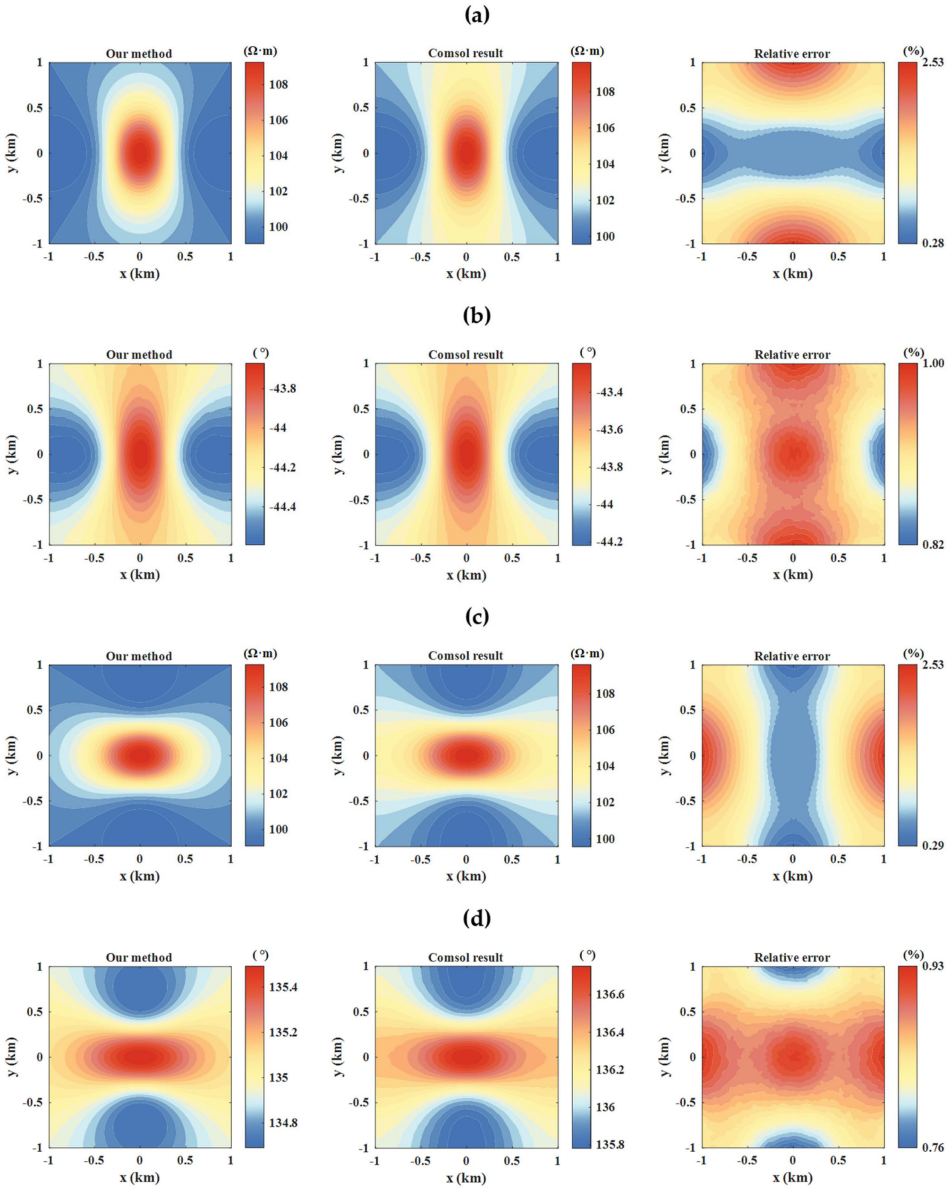


Figure 21. Contour comparison of responses and relative errors between proposed algorithm and Comsol under identical mesh condition. (**a**) ρ^{xy} results comparison, (**b**) φ^{xy} results comparison, (**c**) ρ^{yx} results comparison, (**d**) φ^{yx} results comparison.

4. Conclusions

We develop a three-dimensional MT forward-modeling algorithm based on a mixed space–wavenumber domain approach that combines divergence correction with the Gauss–Legendre Fourier transform. Starting from the frequency-domain Maxwell equations and following established potential-based formulations for electromagnetic induction, we adopt the Lorenz gauge to decouple the vector and scalar potentials, yielding a Helmholtz-type governing system expressed solely in terms of the secondary vector potential. A two-dimensional Gauss–Legendre Fourier transform is applied along the horizontal directions, reducing the original three-dimensional electromagnetic problem to a set of independent one-dimensional ordinary differential equations in the wavenumber domain. This transformation substantially reduces the number of unknowns and the overall computational cost. In the vertical direction, we employ quadratic interpolation finite elements for discretization, which yields a penta-diagonal sparse coefficient matrix. An extended chasing method based on LU decomposition enables a fast solution with linear computa-

tional complexity, O(n). To suppress spurious numerical solutions that commonly arise at electrical-property interfaces, we impose divergence constraints at material boundaries, enforcing the divergence-free condition on the magnetic vector potential. This approach effectively eliminates boundary-related false anomalies in low-induction-number regimes. In addition, a compressed iterative operator is introduced to stabilize the iterative solution for the scattering currents, ensuring robust convergence even in models with strong resistivity contrasts.

We validated the algorithm using the COMMEMI 3D-1 standard benchmark model, a low-resistivity thin-plate model, and a high-resistivity block model. The algorithm's performance was compared against the theoretical responses of COMMEMI 3D-1, as well as against results from the finite-volume method implemented in SimPEG and the finite-element software Comsol Multiphysics. These comparisons confirm both the reliability and computational advantages of the proposed method. The results demonstrate that: (1) the divergence-correction mechanism effectively suppresses false anomalies at the boundaries of anomalous bodies, with the effect being most pronounced at 10 Hz; (2) the Gauss–Legendre Fourier transform substantially reduces spectral truncation errors typically associated with conventional fast Fourier transforms, without requiring additional sampling nodes; (3) under identical mesh discretization, the relative error in apparent resistivity is below 4%, while the phase response error remains within 1%, indicating that the simulation accuracy satisfies exploration requirements; and (4) both computation time and memory usage scale linearly with the number of mesh elements, allowing efficient handling of large-scale models with over eight million nodes. Under fine-mesh conditions, the proposed method achieves approximately 8–10 times improvement in computational speed and memory efficiency compared to the commercial finite-element software Comsol.

The proposed method is a specialized mixed space–wavenumber domain solver for 3D MT forward modeling with laterally uniform/regular horizontal grids and 1D vertical finite-element discretization. It reduces the dimensionality of the problem and enforces the divergence-free condition through a divergence-correction scheme. Numerical tests show good accuracy and linear scaling for the tested regular-grid models. However, because the horizontal FFT requires uniform lateral sampling, the method is not intended to replace unstructured FEM/FVM for rugged topography, arbitrary inclined boundaries, or fully unstructured meshes. Its efficiency advantage is established for regional-scale models with laterally regular grids and target-accuracy comparisons. Extension to anisotropic media and fully unstructured meshes remains future work.

Author Contributions: Conceptualization, T.T. and D.L.; formal analysis, T.T. and Y.Y.; funding acquisition, T.T. and D.L.; methodology, T.T. and Y.Y.; project administration, D. L. and T.T.; visualization, T.T. and Y.Y.; supervision, Y.Y.; writing-original draft preparation, Y.Y.; writing-review and editing, T.T. and Y.Y. All authors have read and agreed to the published version of the manuscript.

Funding: This research is financially supported and funded by the National Key Research and Development Program of China (Grant No. 2022YFC2903704) and National Key Scientific and Technological Project on Deep Earth Exploration and Mineral Resource Survey (2024ZD1002901).

Data Availability Statement: The original contributions presented in this study are included in the article. Further inquiries can be directed to the corresponding author.

Acknowledgments: The authors would like to thank the editors and the two anonymous reviewers for providing comments that substantially improved the paper.

Conflicts of Interest: The authors declare no conflicts of interest.

References

1. Tikhonov, A.N. On determining electric characteristics of the deep layers of the Earth's crust. *Dokl. Akad. Nauk SSSR* **1950**, *73*, 295–297.
2. Cagniard, L. Basic theory of the magneto-telluric method of geophysical prospecting. *Geophysics* **1953**, *18*, 605–635. [CrossRef]
3. Wang, Y.G.; Jin, S.; Dong, H. Multi-level down-sampling scheme for accelerated solution in magnetotelluric forward modelling. *J. Appl. Geophys.* **2021**, *192*, 0926–9851. [CrossRef]
4. Luan, X.; Zhang, W.; Di, Q.; Wang, R.; Li, Y.; Tang, X. Direct synthesis of time domain pseudo-random 3D electromagnetic response with a band-limited source. *J. Appl. Geophys.* **2022**, *200*, 0926–9851. [CrossRef]
5. Zhang, K.; Wei, W.; Lu, Q.; Dong, H.; Li, Y. Theoretical assessment of 3-D magnetotelluric method for oil and gas exploration: Synthetic examples. *J. Appl. Geophys.* **2014**, *106*, 23–36. [CrossRef]
6. Xiao, T.; Liu, Y.; Wang, Y.; Fu, L.-Y. Three-dimensional magnetotelluric modeling in anisotropic media using edge-based finite element method. *J. Appl. Geophys.* **2018**, *149*, 1–9. [CrossRef]
7. Avdeev, D.B. Three-Dimensional Electromagnetic Modelling and Inversion from Theory to Application. *Surv. Geophys.* **2005**, *26*, 767–799. [CrossRef]
8. Miensopust, M.P.; Queralt, P.; Jones, A.G. Magnetotelluric 3-D inversion—A review of two successful workshops on forward and inversion code testing and comparison. *Geophys. J. Int.* **2013**, *193*, 1216–1238. [CrossRef]
9. Mackie, R.L.; Smith, J.T.; Madden, T.R. Three-dimensional electromagnetic modeling using finite difference equations: The magnetotelluric example. *Radio Sci.* **1994**, *29*, 923–935. [CrossRef]
10. Wang, B.; Liu, J.; Hu, X.; Liu, J.; Guo, Z.; Xiao, J. Geophysical electromagnetic modeling and evaluation: A review. *J. Appl. Geophys.* **2021**, *194*, 104438. [CrossRef]
11. Dmitriev, V.I.; Berdichevsky, M.N. The fundamental model of magnetotelluric sounding. *Proc. IEEE* **1979**, *67*, 1034–1044. [CrossRef]
12. Hohmann, G.W. Electromagnetic scattering by conductors in the earth near a line source of current. *Geophysics* **1971**, *36*, 101–131. [CrossRef]
13. Ting, S.C.; Hohmann, G.W. Integral equation modeling of three-dimensional magnetotelluric response. *Geophysics* **1981**, *46*, 182–197. [CrossRef]
14. Wannamaker, P.E.; Hohmann, G.W.; SanFilipo, W.A. Electromagnetic modeling of three-dimensional bodies in layered earths using integral equations. *Geophysics* **1984**, *49*, 60–74. [CrossRef]
15. Wannamaker, P.E. Advances in three-dimensional magnetotelluric modeling using integral equations. *Geophysics* **1991**, *56*, 1716–1728. [CrossRef]
16. Avdeev, D.B.; Knizhnik, S. Integral equation method for 3D modeling of electromagnetic fields in complex structures with inhomogeneous background conductivity. *Geophysics* **2006**, *74*, F89–F94. [CrossRef]
17. Zhang, L.; Yu, P.; Wang, J.L.; Chen, X.; Li, Y. Study of three-dimensional MT forward modeling based on MNS technique. *Chin. J. Geophys.* **2010**, *53*, 2715–2723. (In Chinese) [CrossRef]
18. Ren, Z.Y.; Chen, C.J.; Tang, J.T.; Zhou, F.; Chen, H.; Qiu, L.W.; Hu, S.G. A new integral equation approach for 3D magnetotelluric modeling. *Chin. J. Geophys.* **2017**, *60*, 4506–4515. (In Chinese) [CrossRef]
19. Ma, Y.X.; Hu, J.H.; Liu, Z.L. Application of the group theory in high-efficient 3D EM modeling using integral equations method. *Prog. Geophys.* **2020**, *35*, 1837–1844. [CrossRef]
20. Lines, L.R.; Jones, F.W. The Perturbation of Alternating Geomagnetic Fields by Three-dimensional Island Structures. *Geophys. J. Int.* **1973**, *32*, 133–154. [CrossRef]
21. Mackie, R.L.; Madden, T.R.; Wannamaker, P.E. Three-dimensional magnetotelluric modeling using difference equations; theory and comparisons to integral equation solutions. *Geophysics* **1993**, *58*, 215–226. [CrossRef]
22. Tan, H. Magnetotelluric three-dimensional modeling using the staggered-grid finite difference method. *Chin. J. Geophys.* **2003**, *46*, 705–711. (In Chinese) [CrossRef]
23. Chen, H.; Deng, J.Z.; Tan, H.D.; Yang, H.Y. Study on divergence correction method in three-dimensional magnetotelluric modeling with staggered-grid finite difference method. *Chin. J. Geophys.* **2011**, *54*, 1649–1659. (In Chinese) [CrossRef]
24. Newman, G.A.; Alumbaugh, D.L. Three-dimensional magnetotelluric inversion using non-linear conjugate gradients. *Geophys. J. Int.* **2000**, *140*, 410–424. [CrossRef]
25. Gao, J.; Smirnov, M.; Smirnova, M.; Egbert, G. A Comparison Study of Explicit and Implicit 3-D Transient Electromagnetic Forward Modeling Schemes on Multi-Resolution Grid. *Geosciences* **2021**, *11*, 257. [CrossRef]
26. Coggon, J.H. Electromagnetic and electrical modeling by the finite element method. *Geophysics* **1971**, *36*, 132–155. [CrossRef]
27. Jin, J.M. *The Finite Element Method in Electromagnetics*, 2nd ed.; Wiley-IEEE Press: New York, NY, USA, 2002; ISBN 978-0-471-43818-2.
28. Tang, J.T.; Ren, Z.Y.; Hua, X.R. Theoretical Analysis of Geo-electromagnetic Modeling on Coulomb Gauged Potentials by Adaptive Finite Element Method. *Chin. J. Geophys.* **2007**, *50*, 1349–1364. [CrossRef]
29. Grayver, A.V.; Bürg, M. Robust and scalable 3-D geo-electromagnetic modelling approach using the finite element method. *Geophys. J. Int.* **2014**, *198*, 110–125. [CrossRef]

30. Grayver, A.V.; Kolev, T.V. Large-scale 3D geo-electromagnetic modeling using parallel adaptive high-order finite element method. *Geophysics* **2015**, *80*, E277–E291. [CrossRef]
31. Grayver, A.V. Parallel three-dimensional magnetotelluric inversion using adaptive finite-element method. Part I: Theory and synthetic study. *Geophys. J. Int.* **2015**, *202*, 584–603. [CrossRef]
32. Haber, E.; Ascher, U.M. Fast finite volume simulation of 3D electromagnetic problems with highly discontinuous coefficients. *SIAM J. Sci. Comput.* **2001**, *22*, 1943–1961. [CrossRef]
33. Weiss, C.J. Project APhiD: A Lorenz-gauged A-Φ decomposition for parallelized computation of ultra-broadband electromagnetic induction in a fully heterogeneous Earth. *Comput. Geosci.* **2013**, *58*, 40–52. [CrossRef]
34. Jahandari, H.; Farquharson, C.G. Finite-volume modelling of geophysical electromagnetic data on unstructured grids using potentials. *Geophys. J. Int.* **2015**, *202*, 1859–1876. [CrossRef]
35. Joon-Ho, L.; Tian, X.; Liu, Q.H. A 3-D spectral-element method using mixed-order curl conforming vector basis functions for electromagnetic fields. *IEEE Trans. Microw. Theory Tech.* **2006**, *54*, 437–444. [CrossRef]
36. Liu, R.; Guo, R.; Liu, J.; Ma, C.; Guo, Z. A hybrid solver based on the integral equation method and vector finite-element method for 3D controlled-source electromagnetic method modeling. *Geophysics* **2018**, *83*, E319–E333. [CrossRef]
37. Long, J.B.; Farquharson, C. On the forward modelling of three-dimensional magnetotelluric data using a radial-basis-function-based mesh-free method. *Geophys. J. Int.* **2019**, *219*, 394–416. [CrossRef]
38. Wang, Y.F.; Liu, J.X.; Guo, R.W. Efficient Multigrid Algorithms for Three-Dimensional Electromagnetic Forward Modeling. *Surv. Geophys.* **2025**, *46*, 555–593, Correction in *Surv. Geophys.* **2025**, *46*, 595–596. [CrossRef]
39. Jahandari, H.; Ansari, S.; Farquharson, C.G. Comparison between staggered grid finite-volume and edge-based finite-element modelling of geophysical electromagnetic data on unstructured grids. *J. Appl. Geophys.* **2017**, *138*, 185–197. [CrossRef]
40. Dai, S.K.; Zhao, D.D.; Li, K.; Zhang, Q.J.; Ling, J.X.; Chen, Q.R. Forward modeling of 3D electromagnetic problems using vector and scalar potentials in a mixed space-wavenumber domain. *Chin. J. Geophys.* **2022**, *65*, 404–416. (In Chinese) [CrossRef]
41. Dai, S.K.; Zhao, D.D.; Li, K. Three-dimensional magnetotelluric modeling in a mixed space-wavenumber domain. *Geophysics* **2022**, *87*, E205–E217. [CrossRef]
42. Dai, S.K.; Chen, Q.R.; Li, K.; Ling, J. The forward modeling of 3D gravity and magnetic potential fields in space-wavenumber domains based on an integral method. *Geophysics* **2022**, *87*, G83–G96. [CrossRef]
43. Wang, D.; Guo, R.; Wang, Y.; Liu, Z.; Tian, S.; Chen, X.; Akande, A.A. Plane wave electromagnetic modeling based on Fourier transform in a mixed domain. *J. Appl. Geophys.* **2026**, *251*, 106284. [CrossRef]
44. Tang, W.W.; Li, Y.G.; Liu, J.X.; Deng, J. Three-dimensional controlled-source electromagnetic forward modeling by edge-based finite element with a divergence correction. *Geophysics* **2021**, *86*, E367–E382. [CrossRef]
45. Zhou, J.J.; Hu, X.Y.; Xiao, T.J.; Zhou, J.; Hu, X.; Xiao, T.; Cai, H.; Li, J.; Peng, R.; Long, Z. Three-dimensional edge-based finite element modeling of magnetotelluric data in anisotropic media with a divergence correction. *J. Appl. Geophys.* **2021**, *189*, 104324. [CrossRef]
46. Wang, Y.; Guo, R.; Liu, J.; Li, J.; Liu, R.; Chen, H.; Cao, X.; Yin, Z.; Cao, C. A divergence-free vector finite-element method for efficient 3D magnetotelluric forward modeling. *Geophysics* **2023**, *89*, E1–E11. [CrossRef]
47. Farquharson, C.G.; Miensopust, M.P. Three-dimensional finite-element modelling of magnetotelluric data with a divergence correction. *J. Appl. Geophys.* **2011**, *75*, 699–710. [CrossRef]
48. Yu, G. Divergence Problem in Solution of Direct Method for Three-Dimensional Magnetotelluric Forward Modeling. *Geophysics* **2026**, *75*, 699–710. [CrossRef]
49. Davis, T.A. *Direct Methods for Sparse Linear Systems*; SIAM: Philadelphia, PA, USA, 2006. [CrossRef]
50. Duff, I.S.; Erisman, A.M.; Reid, J.K. *Direct Methods for Sparse Matrices*, 2nd ed.; Oxford University Press: Oxford, UK, 2017. [CrossRef]
51. Zhdanov, M.; Varentsov, I.; Weaver, J.; Golubev, N.; Krylov, V. Methods for modelling electromagnetic fields Results from COMMEMI—The international project on the comparison of modelling methods for electromagnetic induction. *J. Appl. Geophys.* **1997**, *37*, 133–271. [CrossRef]
52. Cockett, R.; Kang, S.; Heagy, L.J.; Pidlisecky, A.; Oldenburg, D.W. SimPEG: An open source framework for simulation and gradient based parameter estimation in geophysical applications. *Comput. Geosci.* **2015**, *85*, 142–154. [CrossRef]
53. Heagy, L.J.; Cockett, R.; Kang, S.; Rosenkjaer, G.K.; Oldenburg, D.W. A framework for simulation and inversion in electromagnetics. *Comput. Geosci.* **2017**, *107*, 1–19. [CrossRef]

Disclaimer/Publisher's Note: The statements, opinions and data contained in all publications are solely those of the individual author(s) and contributor(s) and not of MDPI and/or the editor(s). MDPI and/or the editor(s) disclaim responsibility for any injury to people or property resulting from any ideas, methods, instructions or products referred to in the content.